ABSTRACT

BAILEY, ZACHARY TYLER. Pulse Shape Discrimination with the Pixie-500 Data-Acquisition System and EJ309 Liquid Organic Scintillators. (Under the direction of John Mattingly).

Due to the current shortage of Helium-3, research has been directed towards the development of alternative technologies capable of reliable and efficient neutron detection. Liquid organic scintillators are being investigated as a possible replacement because of their ability to both detect fast neutrons and reject gamma rays in a mixed field of radiation through the use of pulse shape discrimination. Previous research by other investigators has paired the CAEN and Struck waveform digitizers with a variety of liquid organic scintillators to perform digital pulse shape discrimination and time-of-flight experiments. We used the recently developed, 12-bit, 500 mega-sample-per-second (MS/s) XIA PIXIE-500 with two EJ-309 liquid organic scintillators to perform bench-top ^{252}Cf time-of-flight experiments and investigate alternative methods of digital pulse shape discrimination. The results of the time-of-flight experiment are presented and the necessary off-line data cleaning algorithms are described. The three digital pulse shape discrimination methods that were applied include the standard charge integration technique and two alternative methods (based on pattern-recognition and curve fitting) previously investigated by D. Takaku, T. Oishi, and M. Baba. We found the pattern-recognition method achieved the best neutron-gamma discrimination using a quantitative comparison of separation that estimates the neutron/gamma misclassification rate by fitting overlapping Gaussian distributions to the pulse shape parameter distribution. Due to its relative simplicity, the pattern-recognition algorithm could potentially be implemented on a field-programmable gate array (FPGA) enabling real-time neutron-gamma discrimination with low misclassification rates.

Pulse Shape Discrimination with the Pixie-500 Data-Acquisition System and EJ309 Liquid Organic Scintillators

by
Zachary Bailey

A thesis submitted to the Graduate Faculty of
North Carolina State University
in partial fulfillment of the
requirements for the degree of
Master of Science

Nuclear Engineering

Raleigh, North Carolina

2013

APPROVED BY:

_____	_____
Wolfgang Hennig	Robin Gardner

_____
John Mattingly (Committee Chair)

DEDICATION

To my parents.

BIOGRAPHY

Zachary Bailey was born on July 17th, 1988 in Houston, Texas but lived there for only a few years before moving. Since then, he has lived in four states including Florida, Pennsylvania, North Carolina and Tennessee. He finished high school in North Carolina with a strong interest in applied math and physics and attended the University of Tennessee, Knoxville, in the fall of 2006 studying nuclear engineering. After finishing three years at UT, he transferred to North Carolina State and finished his Bachelor of Science degree in Nuclear Engineering in the spring of 2011 and was admitted to North Carolina State's Graduate School studying nuclear engineering with an interest in nuclear security and safeguards.

ACKNOWLEDGMENTS

I would like to thank the North Carolina State Department of Nuclear Engineering, particularly my advisor, Dr. John Mattingly, for the guidance, advice, and mentorship you have given me along the way. I also would like to thank my committee members, Dr. Wolfgang Hennig and Dr. Robin Gardner for their thoughts and feedback and Dr. Hennig's help with the equipment used to complete this work. Finally, I would like to thank my parents and friends for all their support.

TABLE OF CONTENTS

LIST OF TABLES

LIST OF FIGURES

Chapter 1 -- Introduction

1.1 Motivation and Background

Rapid and reliable detection, identification, and characterization of special nuclear material are capabilities essential to nuclear security. Following the dissolution of the Soviet Union (USSR) in the late 1980s, international efforts were made to reduce and safeguard the Russian stockpile of nuclear weapons and materials [1,2]. However, there were numerous confirmed cases of nuclear material smuggling, particularly in former Soviet bloc countries in Eastern Europe during the decade following the USSR's dissolution [3]. It is reasonable to assume that there have also been cases where the smugglers were never caught and the materials were never recovered.

The terrorist attack on United States (US) on September 11th, 2001 reminded the world that terrorism is a very real threat, and extremist groups have since made it clear that they would use a nuclear weapon against the U.S. if they could obtain one [4].

Special nuclear material (SNM) is the essential component of any nuclear weapon, and any of the following elements or isotopes are weapons-usable: plutonium, ^{235}U, or uranium enriched in the isotopes of ^{233}U or ^{235}U [5]. Unlike most other radionuclides, SNM has the unique characteristic in that it spontaneously emits both gamma rays and neutrons, and in sufficient quantities, it can sustain induced fission chain-reactions. This attribute can be used to distinguish SNM from other potentially benign radiation sources if detection methods capable of distinguishing between gamma rays and neutrons are employed.

Historically, ^{3}He gas-filled proportional counters have been one of the primary instruments used to detect neutrons because of ^{3}He's large (n,p) reaction cross-section at low neutron energies and the proportional counters' low sensitivity to gamma rays. However, the supply of ^{3}He is quickly diminishing due to the termination of tritium production [6]. The shortage of ^{3}He has made the development of alternative neutron detection technologies a

high priority in US research and development for domestic and international nuclear security [7].

Organic scintillators represent one possible neutron detection replacement technology for ^{3}He proportional counters for many reasons. Liquid organic scintillators are typically composed of aromatic compounds made with a solute and solvent mixture. The solvent has the highest concentration while the solute has a much lower concentration and its function is analogous to that of the activator that is present in inorganic scintillators [8]. In inorganic scintillators, most of the energy is absorbed in host crystal, but most of the light production occurs in the activator. In organic scintillators the solvent absorbs most of the energy imparted by incident radiation, but almost all of the scintillation occurs in the material of lesser concentration, the solute. The liquid form of these mixtures offers many advantages when compared to other solid detector materials. Liquid organics are relatively easy to manufacture and cost much less than crystalline scintillators; the liquid form also allows them to be used with uniquely shaped detector cells, such as an annulus, that would otherwise be challenging to manufacture using crystalline detector materials. The liquid solution is also many times more resistant to radiation damage than a solid detector with a crystalline lattice, which means liquid organics scintillators can be used in high-flux environments for long periods of time. Occasionally liquid organics are also used in low activity counting applications in which the radioactive material is completely dissolved into the liquid organic solution. This arrangement provides very high detection efficiency because the source itself is integrated with the detector solution [9].

Besides for the physical advantages that liquid scintillators offer, there are also several other intrinsic benefits to using this type of detector. One of their most notable attributes is their sensitivity to many different types of radiation including light and heavy charged particles, gamma rays, and fast neutrons. Since liquid organics are composed almost entirely of carbon and hydrogen, they typically have a density similar to water, so their sensitivity to gamma rays is due almost entirely to Compton scattering, because the photoelectric cross-section is very low for the low atomic number (low-Z) constituents. In some applications, the organic medium has been “doped” with a high-Z element, e.g. tin or

lead, to increase the probability of photoelectric capture and therefore full energy deposition. Experiments have shown, however, this addition can produce a lower light output and therefore decreased energy resolution, which results in performance inferior to that of an inorganic scintillator used for the same application [10].

Fast neutron sensitivity in organic scintillators is primarily due to neutron elastic scattering off hydrogen nuclei, a.k.a. "proton recoil" [11]. In an elastic scatter interaction with a hydrogen nucleus, the incident neutron can transfer all of its kinetic energy to the recoiling proton, which then behaves like a heavy charged particle as it travels through the detector medium. Scattering off carbon nuclei also contributes to the fast neutron sensitivity of organic scintillators, but the light yield from carbon scatter is much lower [12].

Organic scintillators also typically exhibit very fast time response, which results from the short time required to excite the organic molecule and the short time required for the molecule to relax to the ground state via optical photon emission. Scintillation light production in most liquid organic scintillators occurs on the order of nanoseconds. In contrast, most inorganic scintillators produce scintillation light over periods on the order of microseconds [13]. As a result, liquid organic scintillators are some of the fastest detectors available and are very useful in high-count rate and precise timing applications.

One of the most notable and useful characteristics of liquid organic scintillators is their ability to differentiate incident particle types. Frequently, organic scintillators are used to discriminate between fast neutrons and gamma rays in a mixed radiation field. If the accuracy of the particle discrimination is sufficient, liquid organic scintillators could potentially be used to replace ^{3}He neutron counters.

Pulse shape discrimination, or PSD, is the technique typically applied to discriminate between particle types in a mixed radiation field [14]. As its name suggests, PSD uses the *shape* of the light pulse produced by the liquid organic scintillator to discriminate between incident particle types.

Liquid organic scintillators materials used for PSD include EJ301 (a.k.a., NE213 and BC501A), and BC519 [15]. These particular liquid organic solutions are known to be carcinogenic due to benzenoid nature of the constituents, and they also have a low flashpoint

(the flashpoint of EJ301 is 26C). EJ309 was recently developed as an alternative to EJ301; it has a higher flash point (144 C) and it is less toxic than EJ301 (See Appendix Figure A-3). Anthracene has the highest light output per unit energy deposited of any known organic scintillator; EJ309 exhibits light output equivalent to 75% of anthracene's light output for the same incident radiation. EJ309 emits approximately 11,500 photons with a peak wavelength of 424 nm (i.e., blue light) emitted per 1 MeV electron [16] (See Appendix Figure A-3).

Light output in an organic scintillator is linear with the energy deposited by the recoil electron from a Compton scatter interaction, but it is nonlinear with the energy of the recoil proton from a neutron elastic scatter. The light output for protons can be 10 times less than it is for electrons depositing the same amount of energy. To account for the nonlinearity in proton light output, the electron equivalent (ee) unit is used to quantify the light output from liquid organic scintillators. For example, the particle energy necessary to produce 500 keVee of light is 500 keV for fast electrons but is much higher for heavy charged particles due to their reduced light yield.

Although liquid organics scintillators have traditionally been the detector of choice for PSD applications, there has been some success using other types of detectors. Pulse shape discrimination in plastics has previously been shown to be inferior to liquid organic PSD and in some cases, impossible, depending on the plastic chosen. Hybrid detectors that consist of a combination of plastic and liquid scintillators have been shown to have efficient neutron-gamma pulse shape discrimination capabilities [17]. Captured-gated scintillators, such as BC-523A, have also shown promising PSD results. Capture-gated scintillators are comprised of a plastic or liquid organic material doped with a material such as Li-6, which has a high (n, α) cross-section. In a typical liquid organic scintillator, such as EJ309, neutron interaction occurs primarily via proton recoil. Capture-gated scintillators use a dopant with a high (n, α) cross-section to capture the neutron that initially scattered off the hydrogen nucleus, which thereby produces a second scintillation pulse correlated in time with the first pulse. In this way, one neutron can cause two light pulses in a capture-gated scintillator and a neutron interaction can be and differentiated from a gamma ray interaction by the timing of the second "capture" pulse after the initial "scatter" pulse [18].

More often, PSD exploits the fact that the light pulse from heavy particles decays more slowly than the pulse from light charged particles. This phenomenon is called delayed fluorescence, or phosphorescence. Historically, pulse shape discrimination was performed using a series of analog pulse shaping circuits. The analog pulse-shaping networks typically consisted of several sequential RC and CR circuits. An analog PSD technique that has been frequently applied is called "cross-over" analysis. This method employs a bipolar pulse-shaping network consisting of a CR-RC-CR circuit network. The time interval between the start and the zero crossing of the bipolar pulse is determined by the input pulse's tail shape and is used as the pulse shape parameter to classify particles [19]. Another frequently applied analog PSD technique is called "charge integration". The charge integration method uses the fact that the fraction of total light produced during "slow" component of decay from a liquid organic scintillator depends on the nature of the particle that caused it. For a neutron interaction, the recoil nucleus will produce a greater fraction of the total scintillation light to be emitted during the slow decay component than would be observed from a gamma interaction of equivalent energy deposition. The charge integration method integrates the pulse over both the entire duration of the pulse and over the duration of the pulse's tail to determine how what fraction of light was produced in the tail. The incident radiation type is determined from the ratio of the tail area to total area [20].

While analog pulse processing systems require physical circuits to perform specific shaping algorithms, recently developed digital pulse processing systems employ analog-to-digital conversion to digitally sample pulses. Digital PSD methods fall into one of three categories including: (1) integrating the charge over different areas of the pulse, (2) detecting fall time changes of the output pulse, and (3) fitting the output pulse with different functional forms [21]. The first method, digital charge integration, is essentially a digital implementation of the analog charge integration method. The principal problem with the charge integration method (both analog and digital) is that it often misclassifies low-energy neutrons as gamma rays. The second technique, digital crossover, is a digital emulation of the analog crossover method. It relies on very slight differences between the pulse tail decay times for neutrons and gammas in liquid organic scintillators, and it differentiates particle

type based on where the pulse crosses zero after it has been digitally shaped into a bipolar pulse. This method has been shown to be effective, but can fail to detect very small differences in tail decay times for neutrons and gamma rays [22]. The third method involves a shape analysis of an output pulse. A common shape characteristic to analyze is the tail decay constant; since neutrons pulses decay slower in time than gamma pulses do, there will often be a difference in tail decay constants for neutrons and gamma rays. This method, known as the curve-fitting method, has been shown to effectively differentiate between neutrons and gamma rays with only one shape parameter used to describe the decay of pulse [23].

1.2 Thesis Contents/Scope of Work

Included in this work are the experimental methods, analysis methods, and results of three separate digital pulse shape discrimination methods including:

- Digital charge integration
- Pattern recognition
- Curve fitting procedure

All three methods provide good neutron and gamma ray discrimination and have previously been shown to be effective. Typically, a time of flight (TOF) measurement is conducted with a mixed source of radiation that emits neutrons and gamma rays, such as Cf-252, prior to any pulse shape discrimination research to provide a basis on which to judge the accuracy of the PSD algorithms [24]. A time-of-flight measurement classifies particles based on the time it takes them to travel a known distance between a "start" and "stop" detector. Since gamma rays travel at the speed of light and neutrons travel at a speed according to their kinetic energy, it will take a neutron much longer to travel the distance between the start and stop detectors. The same data can be analyzed using pulse shape discrimination algorithms; the results of which are compared to the time of flight measurement results. It should be noted however, the time of flight measurement cannot be 100% accurate due to scattered gammas, accidentally coincident gammas, and delayed source gammas, all of which can lead to a gamma ray having an artificially large time of flight, and consequently being misclassified as a neutron. These accidental misclassifications occur relatively infrequently so the TOF measurement still provides a good comparison for results obtained by pulse shape discrimination methods. The results of both the time-of-flight measurement and pulse shape analysis methods will be compared and contrasted to each other in this report.

A common way compare pulse shape discrimination methods is by defining a figure-of-merit. Typically, the figure of merit is generated from a histogram of the pulse shape parameter of interest. The histogram will exhibit two peaks centered on the average shape parameter for each particle type. The distance between these peaks is calculated and used as a metric of quality for the pulse shape discrimination method [25]. In this work, however, the

figure of merit defined uses a Gaussian fitting procedure that calculates the point at which the two Gaussian fits intersect. It uses this intersection to determine the area overlap between the distributions, which is the particle misclassification rate, i.e. the frequency of either particle type being incorrectly classified.

The contributions of this work are:

- This work was performed using the recently developed Pixie-500, a 500 MHz, 12-bit, digitizer and (2) EJ309 liquid scintillators
- The experimental methods and results of a bench-top ^{252}Cf time-of-flight experiment
- 3 pulse shape discrimination algorithms are applied to the TOF experiment data, these algorithms include:
    - A digital charge integration method
    - A pattern recognition method
    - A curve fitting method
- The quality of each PSD method is determined using a figure of merit based on a Gaussian fitting procedure which computes the particle misclassification rate from the distribution of neutron and gamma pulse shape parameters

Chapter 2 -- Digital Pulse Processing and PSD Theory

2.1 Analog-to-Digital Converters

The development of high-speed analog-to-digital converters (ADCs) has been an integral part of the advancement of digital pulse processing systems for radiation detection. Starting in the early 1990s, the development of high-speed waveform digitizers became more widespread and digital pulse shape discrimination was introduced. The ADCs enable complete digitization of each radiation interaction pulse, capturing individual waveforms, timestamps, and pulse heights on an event-by-event basis; consequently they can provide significant advantages over the older analog pulse processing techniques [26]. ADCs provide a high degree of signal stability that is not possible using the old analog pulse processing techniques; once the ADC has converted the analog signal to an equivalent digital signal, it can no longer be altered and is not affected by voltage drifts or temperature changes which can affect analog pulse processing systems. In addition, pulse shaping and can be difficult to implement using analog circuits, but it is easily implemented with digital algorithms. The ADC preserves the analog pulse information sent from the detector during the charge collection time by sampling the amplitude of the pulse many times through its duration. The samples are converted into a series of digital values that are proportional to the analog magnitude of the sample. These digital values can be altered through simple, or complex, mathematic operations in order to digitally shape the pulse [27].

The time and voltage resolution of the ADC dictates its capabilities and which applications it can be used for. The frequency at which the ADC converts the analog signal to digital is based on the sampling rate; a 500 MHz ADC will sample a waveform once every 2 nanoseconds, i.e. it and collects 500 Mega-samples per second (MS/s). Digital pulse shape discrimination requires ADCs with high sample rate and good voltage resolution so that small pulse shape differences can be detected. The ADC voltage resolution, or bit depth, is the number of digital values that are used to represent the analog voltage during the

conversion process. Recently developed ADCs with good resolution have 10 or 12 bits allowing 1024 or 4096 different digital values to represent an analog voltage signal. A 12-bit ADC has a digital resolution of 1/4096, or about .024%, for voltages that are within the input range of the digitizer [28]. Recently developed ADCs operating at 500 MS/s to 1 GS/s with 10 to 12-bit precision have proved to be very useful in digital pulse processing systems and pulse shape discrimination analysis.

2.2 Pixie-500 Operation

The Pixie-500 is a 500 MS/s, 12-bit waveform digitizer designed and manufactured by XIA LLC. The digitizer is a CompactPCI/PXI[12] card, or module, with 4 input channels allowing for digitization of waveforms on each channel with a maximum recording window of 16 microseconds. A commercial PXI crate can house up to 18 PCI/PXI cards thus allowing 72 detectors to be to be utilized in complex detector arrays. The waveforms, timestamps, and energy information of each event is recorded in a manufacturer-specific binary list mode format, which can be accessed with user code after data acquisition for offline processing of the data. The family of Pixie spectrometers was originally designed for high precision gamma ray spectroscopy with high purity germanium detectors, but has since been used with other detectors such as sodium-iodide (NaI), cesium-iodide (CsI), and bismuth germinate (BGO). It can also be used for coincidence spectrometry within the same module or between multiple modules allowing for complex hit patterns between up to 16 channels to be recognized. The Pixie-500's 12-bit, 500 MS/s ADC can also be used for pulse shape discrimination applications that utilize fast response liquid organic scintillators, such as EJ309, and was chosen as the digitizer to conduct this research.

The Pixie-500 has 4 main constituents that comprise its front-end data acquisition system. Figure 2-1 (courtesy of XIA) shows a functional block diagram of the signal-processing module.

[1] Peripheral Component Interconnect (PCI)
[2] PCI extensions for instrumentation (PXI)

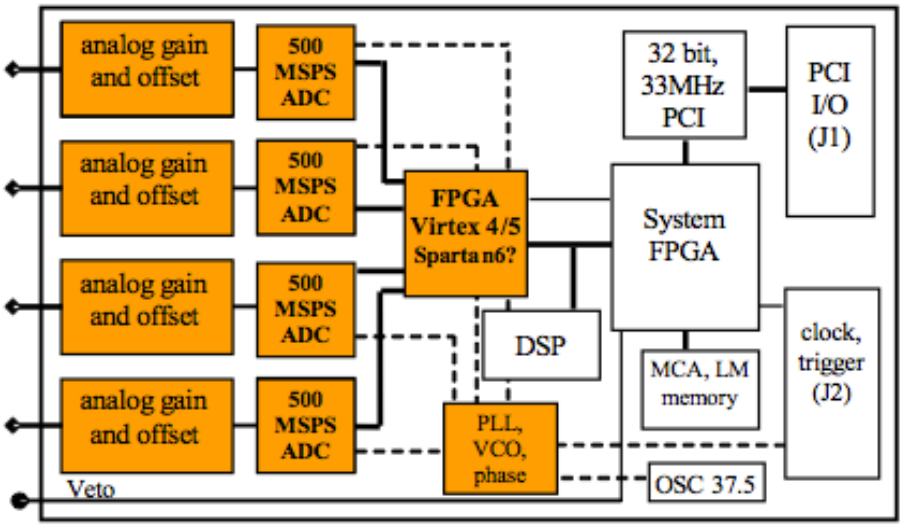

Figure 2-1: Pixie-500 Front End Signal Processing Card [29]

The analog signal sent from the detector is first conditioned so that it is within the input voltage range of the ADC (2 volts). The signal conditioning is performed in the 'analog gain and offset' stage shown in Figure 2-1. The input signals are adjusted for direct current (DC) offsets and sent through a computer controlled gain stage to ensure they fall within the ADC's voltage range. After the signal conditioning, the signal is sent to the ADC where it is digitized at a rate of 500 MS/s before being sent to the field programmable gate array (FPGA). An FPGA acts like a processor that would be found in a personal computer; however, unlike a CPU, an FPGA is reprogrammable to suit different purposes and the number of processing cores available does not limit operations. Since FPGAs are designed to have parallel functionality, different operations do not compete for the same processing resources [30].

The Pixie-500's FPGA applies a digital trapezoidal filter to shape the waveform sent from the ADC. This process is a digital emulation of the analog shaping process that an amplifier performs using CR and RC circuits. Compared to a traditional analog amplifier

circuit filter, a digital trapezoidal filter makes the measurement of pulse height less sensitive to signal shape variations [31].

The FPGA also serves as a pulse pile-up inspector. Pulse pile-up occurs when a pulse is detected to soon after its preceding pulse and effectively "piles-up" on the trailing edge of the preceding pulse. This phenomenon often occurs during high-count rate applications, the FPGA has pile-up rejection logic that is used to reject pile-up events. If a pulse occurs too soon in time after the preceding pulse, the FPGA logic will corrupt the first pulse height measurement and both pulses will be rejected as pile-up. Prior to pileup inspection the FPGA uses leading edge threshold trigger logic that requires the pulse to cross a minimum amplitude threshold, which can be set by the user. If the threshold requirement is satisfied, the pileup inspection will be performed and events will be rejected if the pileup requirements are not met.

If the pulse satisfies both the pile-up and threshold trigger requirements, a trigger is sent to the digital signal processor (DSP). The "first in first out" (FIFO) memory has at this point been filled with the waveform data from the ADC. The FIFO will remain filled until the DSP responds to the trigger and reads the waveform data, timestamps, and raw pulse height data. If a trigger is issued and all user specified requirements are met, an interrupt signal will be sent to the DSP that directs it to read the data from the FPGA, process it for pulse height, and store it in an onboard local memory buffer.

Before the data acquisition run starts, the DSP initializes system variables and sets user-specified requirements such as coincidence windows, trigger thresholds, filter types, and shaping times. The DSP applies timestamps using a 125 MHz clock, records pulse heights, and prepares the data for output to the host PC.

The system FPGA is used for interface logic between the DSP and the 33 MHz PCI interface chip that communicates with the host computer using a direct memory access channel. The direct memory access channel allows the system to read and write data to the DSP memory while data is being acquired, i.e. it reduces dead time during I/O operations.

One particularly important user-specified requirement is the coincidence window. In coincidence mode, the DSP will perform a coincidence test in which it monitors the required

hit pattern and compares it to the one received. If hits are received on the required channels within the specified coincidence window, the coincidence test is passed and data is saved to the local (onboard) memory buffer.

After all logic and user specified requirements are met, the waveform and its data are temporarily stored in the local memory buffer and then moved to an external memory buffer. When the external memory buffer is filled the data acquisition is paused, and the data stored in the external memory buffer is read out to the host PC in a fast block read which typically takes about 30 ms. After the temporary data acquisition halt, the DSP returns to processing waveform data from the external buffer.

In this manner, the Pixie-500 digitizes and writes data to disc. The data is written in a specific binary format that allows the transfer of large amounts of information in a short time period (up to 100 Mega-bytes per second). The data can be accessed with user code for post-processing and analysis.

2.3 Pulse Shape Discrimination

The generation of light in organic scintillators occurs due to molecular transitions. Pulse shape discrimination using certain liquid organic detectors is possible due to the nature of Π-electron structure observed in the bonds that hold the organic molecule together. The Π- electronic structure consists of a series of two levels which are known as singlet and triplet excited states. The Π-electron structure is shown in Figure 2-2.

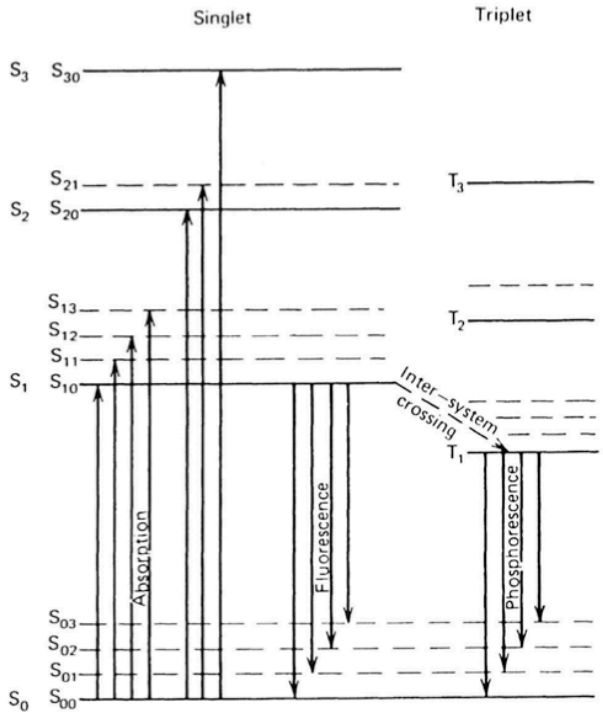

Figure 2-2: Π-Electron Structure (taken from Knoll) of an Organic Molecule [32]

In the figure, the singlet states are denoted S1, S2, S3, while the triplet states are denoted T1, T2, T3. Note that the energy levels for the triplet states are lower than that of the singlet states and thus triplet state de-excitation occurs at a longer wavelength than singlet state de-

excitation does. The dashed lines represent sublevels between excited states, which are different vibrational states that the molecule can exhibit. Singlet states exhibit a net electron spin of 0 while triplet states exhibit a net electron spin of 1. Typically, singlet states de-excite within nanoseconds through fluorescence, while triplet states exhibit delayed fluorescence, or phosphorescence. Through an electronic spin conversion process called intersystem crossing, some molecules can transition from the singlet state to the triplet state prior to de-excitation as shown in Figure 2-2 [33]. The number of electrons that undergo the intersystem crossing to the triplet state is proportional to the linear energy loss per unit distance, dE/dX, of the exciting particle. This means that heavy charged particles will cause a higher density of triplet states to be populated and thus cause a greater fraction of light to be produced through phosphorescence [34]. This phenomenon produces a pulse shape, which depends on the incident particle type. A neutron interaction will produce a proton, which causes a pulse that decays more slowly in time than a pulse caused by an electron as a result of a gamma interaction. Figure 2-3 shows a typical gamma and neutron waveform generated in EJ309; the shape shown is a result of averaging many pulses.

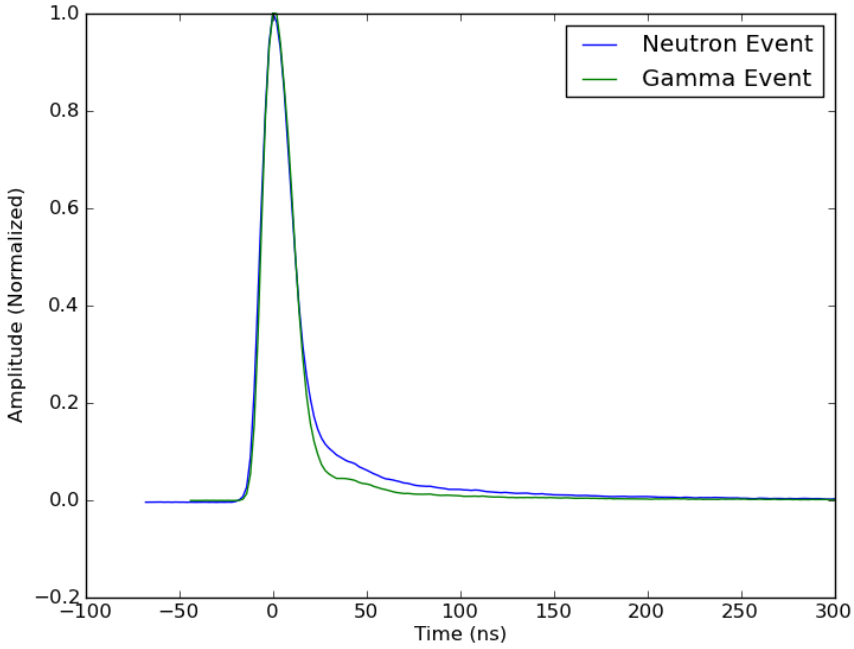

Figure 2-3: Neutron and Gamma Events in EJ309

The figure shows the distinct shape difference of a neutron and gamma waveform, which is the basis for pulse shape discrimination. The time-dependence of light output can be represented by the sum of two exponential decay terms; these are often referred to as the "fast" and "slow" components of scintillation decay. The pulse shape difference shown in Figure 2-3 can be exploited in a variety of ways to perform pulse shape discrimination as described in Chapter 1.

Chapter 3 --Experimental Methods and Results

3.1 Setup and Preliminary Testing

Prior to any pulse shape discrimination research, the instruments used for the investigation were thoroughly characterized and tested for performance and functionality. The equipment that was tested and used is shown below in Table 3-1.

Table 3-1: Instruments and Equipment

Instrument	Manufacturer	Model Number
(2) High Voltage Supply Box	Stanford Research Systems	PS350\5000V-25W
5x5 EJ309 Liquid Organic Scintillator	Eljen	510-50x50-9\309
3x3 EJ309 Liquid Organic Scintillator	Eljen	510-30x30-5\309
Photomultiplier Tube (5x5)	Hamamatsu	R1250
Photomultiplier Tube (3x3)	Etell	**
Fast Waveform Digitizer	XIA- National Instruments	Pixie-500
Signal Delay Box	Ortec	DB463
Oscilloscope	Tektronix	DPO2012
Waveform Generator	Tektronix	AFG3101

The equipment testing and pulse shape discrimination research were performed in a sequential manner. The testing began with the simplest arrangement of equipment and progressed through successively complex arrangements that were more representative of the research requirements. The results were verified and recorded before moving to the next stage of testing. The first testing procedure involved verifying the functionality of the liquid organic scintillators. The Eljen 3x3 and 5x5 scintillators are fitted with similar, but not identical, fast photomultiplier tubes (PMTs) that collect the visible photons generated in the

scintillators and convert them to an electrical signal. The PMT dictates the voltage at which the detector is operated at, and the manufacture recommended that the 3x3 and 5x5 be operated with negative polarity at 1825 volts and 1525 volts, respectively. Each detector was tested individually by connecting the anode output to the Tektronix digital oscilloscope with an RG-58 signal cable. A 50-Ohm terminator was connected in parallel with the cable connection on both ends to match output and input impedances. A typical pulse acquired on the scope from a ^{137}Cs source is shown in Figure 3-1.

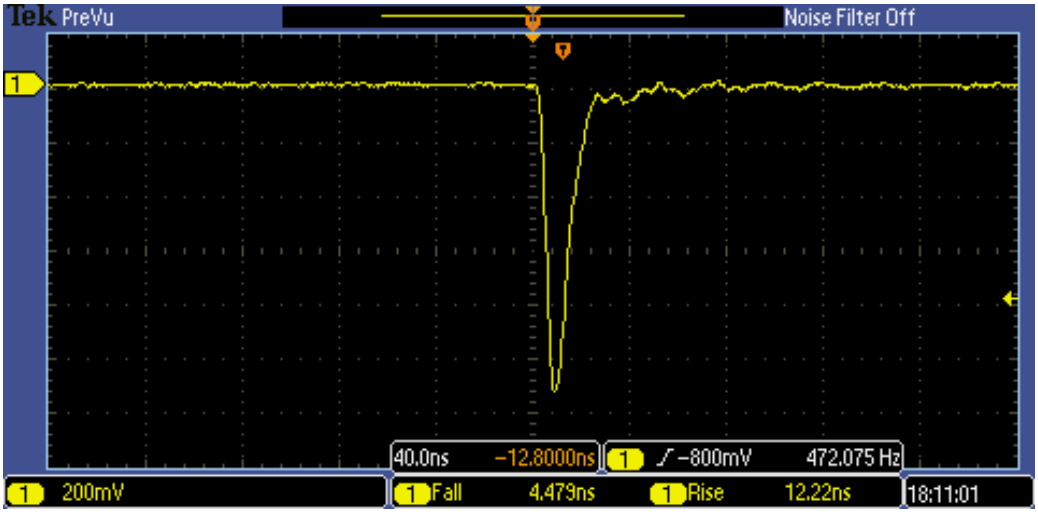

Figure 3-1: A Typical EJ309 Output Pulse

The figure shows a typical pulse output by the 3x3 EJ309 anode that has approximately a 4.5-nanosecond fall-time, a 40-nanosecond width, and a 12-nanosecond rise time. The 5x5 EJ309 also output a pulse similar to the one shown in Figure 3-1.

The next step was to confirm that the Pixie-500 produced a digital pulse similar to the one shown by the oscilloscope in Figure 3-1. The Pixie-500 operating manual was consulted in order to choose the proper configuration for the digitizer settings and a series of list mode data acquisition (DAQ) runs were performed. List mode DAQ records information on an

event-by-event basis including the digitized waveform, timestamp, and event energy. This data is recorded in a manufacture-specific binary format and saved to disc for offline post-processing.

The Pixie-500 also includes an onboard digital oscilloscope that is used to examine waveforms prior to data acquisition. After the run has concluded, individual pulses can be examined using the graphical user interface's 'list mode traces' display function. Figure 3-2 shows a typical digital trace displayed using the list mode trace function in the graphical user interface (GUI).

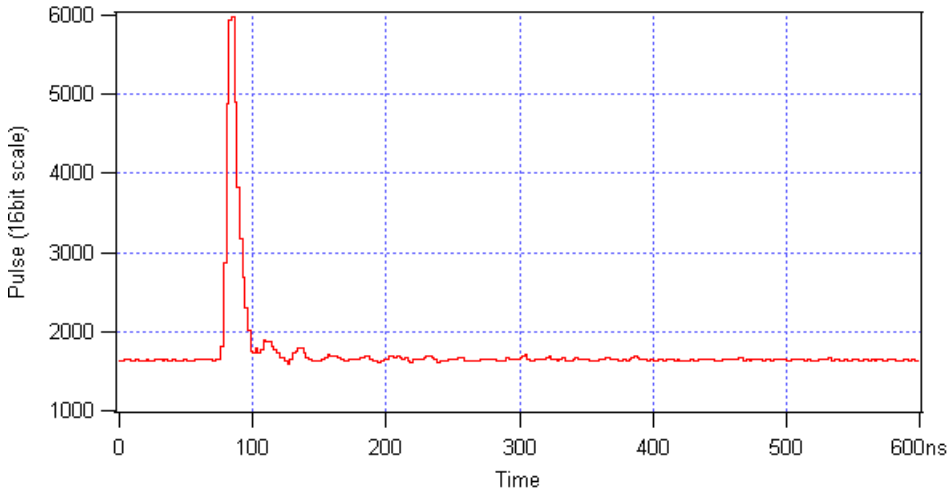

Figure 3-2: A Typical Digitized Pulse from EJ309

After examining the figure, there are several details we can note. First, the pulse has been inverted using the 'invert pulse' function on the onboard oscilloscope. The waveform was recorded for a 600 ns window with a pre-determined 'trace delay'; these settings were chosen prior to the data acquisition. A 600 ns recording window was used for all subsequent measurements.

3.2 Radio Frequency Noise Mitigation

After testing the detectors and the Pixie-500 for functionality, a post-processing algorithm was developed to read and analyze waveforms after the data was collected. For this work, all post-processing algorithms were developed with Python, an object-oriented scripting language. A pulse extracted by the offline post processing script is shown below in Figure 3-3.

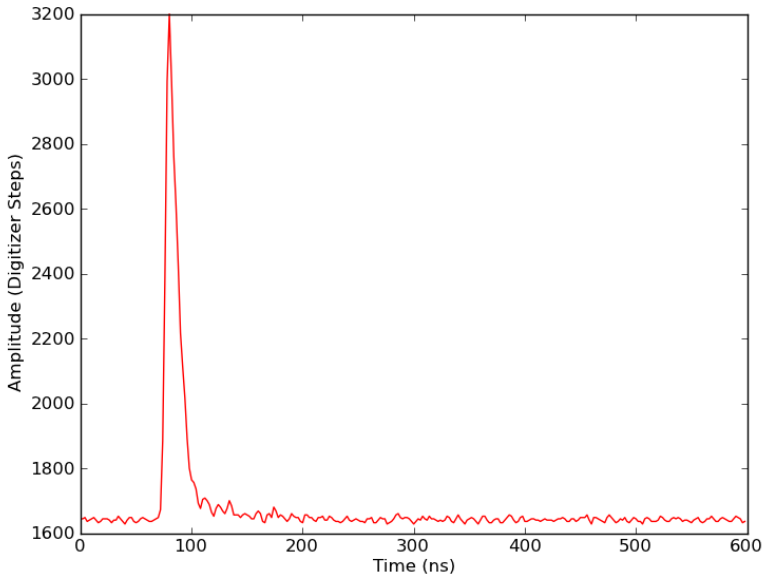

Figure 3-3: A Typical Digitized EJ309 Pulse (In Lab)

This pulse was collected in the lab and shows a sinusoidal oscillation about the baseline, both before and after the peak, which could lead to inaccurate pulse shape analysis. At this point a series of noise mitigating procedures were implemented in an attempt to minimize the high frequency oscillations about the baseline before and after the pulse.

Proper care was taken to ensure that all components used for measurements had matching impedance. Impedance is a measure of the overall resistance to current flow when an applied voltage is moving across the path of the current. Impedance matching can be achieved by using an appropriate coaxial signal cable with characteristic impedance that matches the input impedance of the digitizer. The Pixie-500 was set to have an input impedance of 50 ohms by configuring the proper jumpers on the hardware, which ensured matching impedance with the 50-ohm RG58 signal cables used.

A common problem in signal processing is a phenomenon known as ringing; ringing is the unwanted oscillation of a signal caused by signal reflection. In order to prevent signal reflections, a terminator with the same impedance must be placed at the PMT anode end of the cable. The terminator's impedance should match the cable's impedance, which allows the terminator to act like an infinitely long cable and prevent signal reflections that are due to abrupt changes in the medium through which the signal is propagating. To minimize ringing and signal oscillations the following steps were taken:

- Impedances were matched across all components of the experiment
- Terminators were used where appropriate
- PMTs that were manufactured to minimize ringing (Refer to Appendix) were used
- Ferrite blocks were used to attenuate high frequency noise

After these steps were taken, the waveforms still exhibited some high frequency noise.

To further investigate the cause of the noise, a Fast Fourier Transform (FFT) analysis of the waveforms collected was performed. An FFT analysis transforms the signal from the time domain to the frequency domain, allowing the decomposition of the waveform in terms of the frequencies that it is composed of. This analysis can determine how much information is contained in the waveform at certain frequencies and is important when analyzing signal noise sources. The FFT analysis can be used to generate a power spectrum, which provides a plot of a signal's power as a function of frequency, and it can be used to pinpoint the frequency of interference [35]. The power spectrum for the waveforms collected in the lab is shown in Figure 3-4.

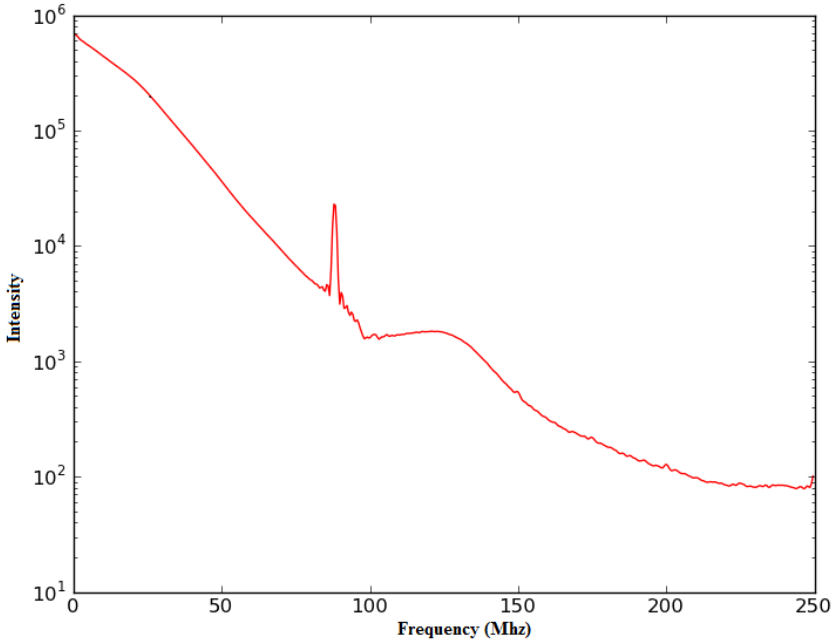

Figure 3-4: Signal Power Spectrum (In Lab)

This power spectrum shows a significant amount of interference at a frequency of 88.1 MHz. North Carolina State University's radio station broadcasts at this frequency, and the RG58 cables act like an antenna, allowing the radio waves to interfere with the detector signal. We attempted to use a digital low-pass filter algorithm to remove the 88.1 MHz noise, but it significantly altered the pulse shape.

A common way to eliminate RF interference is to use a Faraday cage. A Faraday cage acts as a shield against electromagnetic radiation, such as FM radio waves, and is essentially an enclosure that is electrically grounded with a fine mesh screen surrounding it. Figure 3-5 shows a power spectrum from waveforms that were collected inside the Faraday cage.

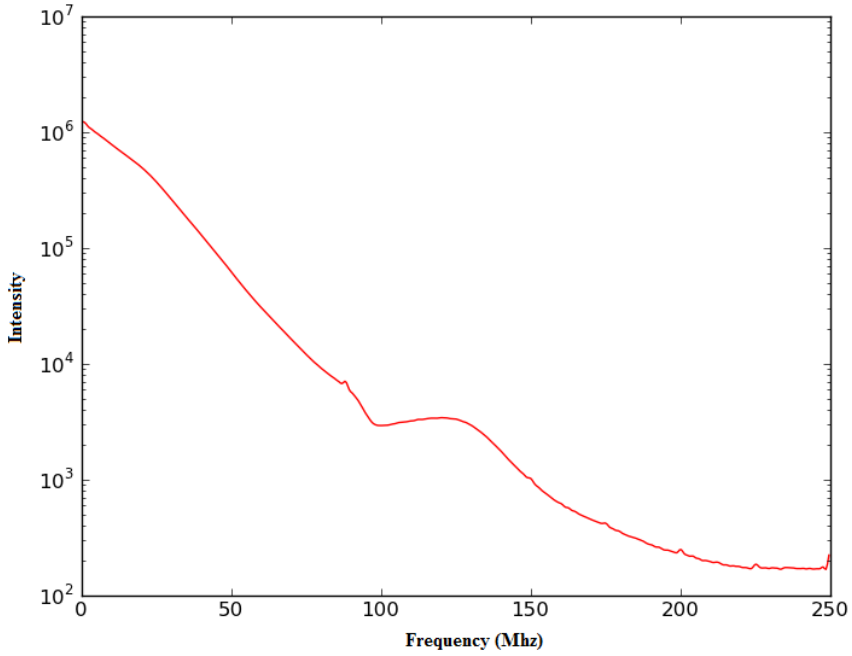

Figure 3-5: Signal Power Spectrum (In Faraday Cage)

The power spectrum shows that the RF interference is almost completely eliminated by the Faraday cage. Figure 3-6 shows a waveform that was collected in the Faraday cage.

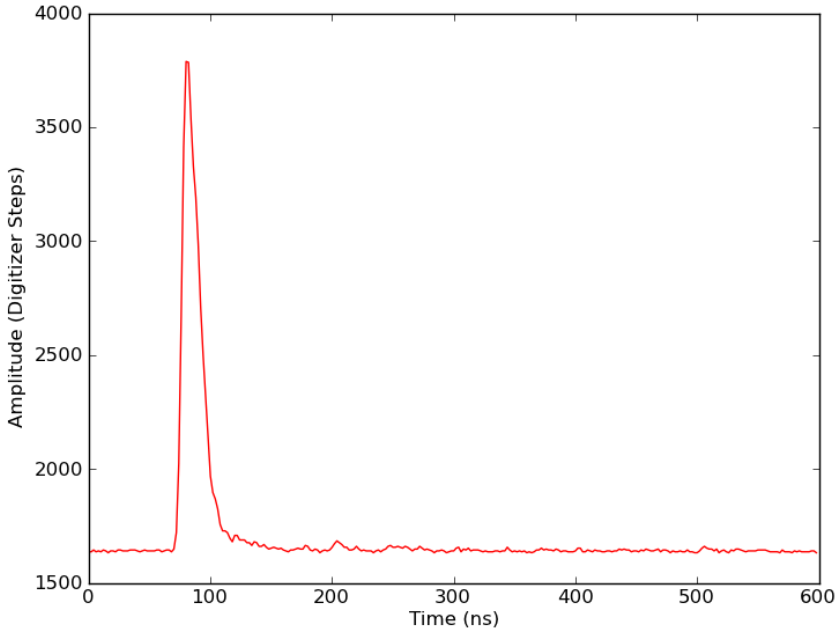

Figure 3-6: A Typical Digitized Pulse (In Faraday Cage)

The figure shows that the oscillation about the baseline is almost completely eliminated as a result of the Faraday cage. Consequently, the remaining experiments were conducted in the cage to mitigate the RF interference problem.

Chapter 4 -- Implementation of Alternative Pulse Shape Discrimination Techniques

This chapter of the thesis describes the implementation of several alternative digital pulse shape discrimination techniques including:

- Charge integration
- Pattern recognition
- Curve fitting

The implementation of each technique is described, and each technique's ability to discriminate gammas from neutrons is compared to a "ground truth" classification of particle type obtained from a time-of-flight measurement with Cf-252. In addition, the performance of each technique is evaluated by estimating its particle misclassification rate from the distribution of gamma and neutron pulse shape parameters.

4.1 Energy Calibration and Pulse Height Threshold

Charge integration PSD tends to exhibit a high misclassification rate for low-amplitude pulses, and the other methods of PSD described in this thesis exhibit the same problem. In each case, the problem is one of signal-to-noise: for low-amplitude pulses, the pulse tail rapidly falls below the electronic noise (typically radio frequency noise), such that it becomes very challenging to sense the small differences in pulse decay characteristic of gammas and neutrons. Consequently, a lower threshold on pulse height was set before applying each of the PSD algorithms. Figure 4-1 shows the pulse height distribution (PHD) acquired from ^{137}Cs using the 5x5 EJ309 liquid scintillator.

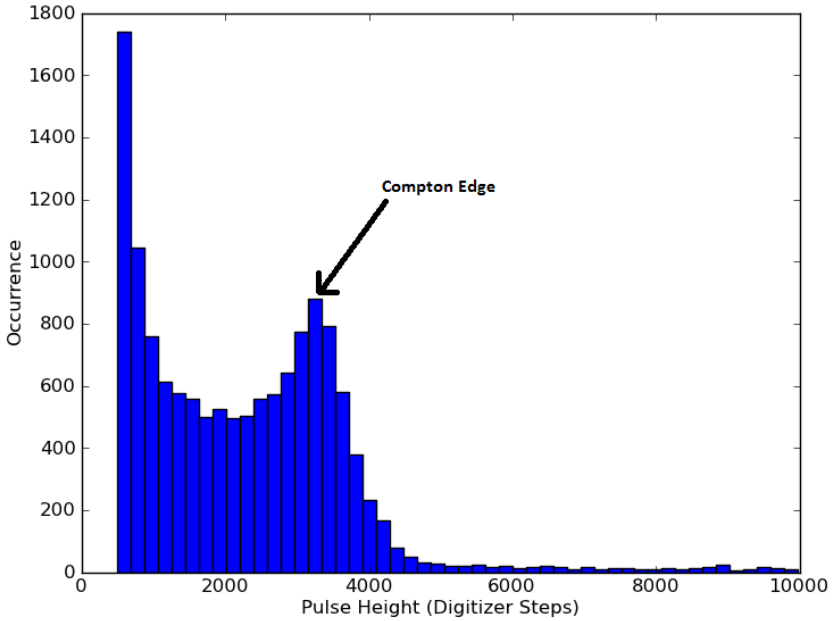

Figure 4-1: Pulse Height Distribution for a ^{137}Cs Source

The figure shows a prominent Compton continuum but the PHD lacks a full-energy peak. Full energy deposition is rare in EJ309 because of the low atomic number of the constituents [36]. The location of the Compton edge can be used to relate recoil electron energy to the scintillator light output (pulse height).

The Compton continuum occurs due to incident photons deflecting off orbital electrons at random scattering angles. A gamma ray will transfer a fraction of its incident energy E to the recoil electron and will emerge with an energy E'. The energy of the gamma ray after the collision is a function of photon scattering angle θ:

$$E' = \frac{E}{1 + \frac{E}{m_e c^2}(1 - \cos\theta)} \tag{4.1}$$

where $m_e c^2$ is the electron rest mass, 511 keV. The location of the Compton edge corresponds to a photon scattering angle of 180 degrees, i.e., a near head on collision with an

electron, which transfers the maximum portion of photon energy to the recoil electron. Assuming the recoil electron is initially at rest, its energy as a result of the collision can be given as a function of the photon's energy before and after the Compton scattering interaction. The recoil electron energy is:

$$E_{e^-} = E - E' \tag{4.2}$$

where again E is the incident photon energy and E' is the emergent photon energy. The location of the Compton edge, or the maximum recoil electron energy, is obtained in two steps using equations (4.1) and (4.2). Evaluating equation (4.1) with a scattering angle of 180 degrees and an incident photon energy of 662 keV, for ^{137}Cs, results in the minimum emergent photon energy, E', of 184 keV. Equation (4.2) can then be evaluated with incident photon energy of 662 keV and emerging photon energy of 184 keV to obtain the maximum electron recoil energy of 478 keV, which is the energy at which the Compton edge is located. Figure 4-1 shows the location of the Compton edge of a ^{137}Cs source in terms of digitized pulse height. The pulse height represents the light output of the EJ309 scintillator, which is linear with the energy deposited by a recoil electron, and can be related to the energy deposition using equation (4.3).

$$\frac{478 \text{ keV}}{\text{Digitized Pulse Height at Compton Edge}} = \frac{\text{Recoil Electron Energy (keV)}}{\text{Digitized Pulse Height}} \tag{4.3}$$

Figure 4-1 shows the Compton edge is located in digitizer channel 3279. Using equation (4.3), a recoil electron of 100 keV will occur in digitizer channel 686. Both detectors were gain matched so that the Compton edge occurred at approximately the same location ensuring equal thresholds for both the 3x3 and 5x5 EJ309.

Since the scintillator light output for a recoil proton and a recoil electron of equivalent energy is not equal, the term keVee, or keV electron equivalent, is used to place the light output on an absolute basis. A 100 keV electron will produce 100 keVee of light output (1 to 1 ratio); a recoil proton of equivalent energy will produce a smaller light output [37].

The nonlinear light production of EJ-309 due to a given amount of energy deposited by a proton has been determined empirically. The University of Michigan (UM) has

conducted experiments to characterize the light output of EJ309 [38,39] and their results are shown in Figure 4-2.

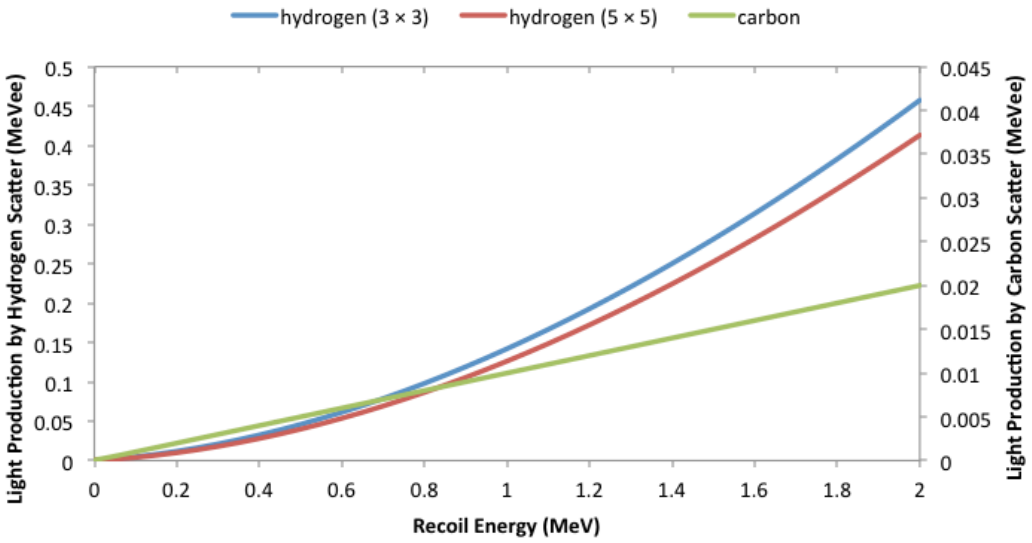

Figure 4-2: EJ309 Light Output

The figure shows the light output due to neutron scattering off both hydrogen and carbon for a 3x3 and a 5x5 EJ309 liquid scintillator. The light output due to a carbon scattering interaction is much lower than it is for hydrogen and is fairly linear with recoil energy. The light output, L, in MeVee (MeV electron equivalent), for the 5x5 due to a hydrogen scatter can be described by equation (4.4).

$$L = aE_p - b\left[1 - \exp\left(-cE_p\right)\right] \tag{4.4}$$

where, E_p is the recoil proton energy in MeV, and *a*, *b*, and *c*, have been measured by UM to be 0.74787, 2.4077, and 0.29866, respectively. Using these results, it was determined that 100 keVee corresponds to 900 keV of energy deposited by the recoil proton; consequently, the gamma lower threshold was 100 keV and the neutron lower threshold was 900 keV.

4.2 Time Pick-Off Method

A triggering algorithm was implemented to resolve the arrival time of each pulse. There are two timing mechanisms that were used to calculate the arrival time of a pulse. The first is the Pixie-500's internal 125 MHz 16-bit clock, which assigns trigger timestamps to each waveform in 8 ns periods; every increment of the clock represents one 8 ns cycle. The second timing component used to determine arrival time was an offline digital constant fraction discriminator (CFD) algorithm, used to determine the peak time of each waveform within the 600 ns recording window.

Constant fraction discrimination is a time pick-off (a.k.a., triggering) method designed to accurately determine arrival times of pulses with the same rise time but varying height. Using simple leading edge threshold triggering, pulses with identical rise times and varying pulse heights can cause a trigger time dependence on pulse amplitude, called amplitude walk [40]. A CFD is designed to produce trigger times that are independent of pulse amplitude. The digital CFD used in this work was previously implemented with Pixie hardware and has been shown to be effective [41]. Figure 4-3 shows a typical implementation of the digital CFD.

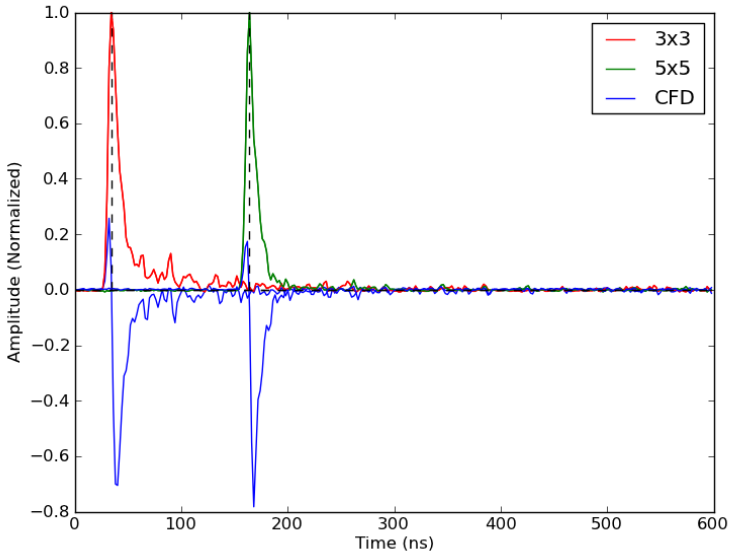

Figure 4-3: Digital Constant Fraction Discriminator

The CFD is constructed by subtracting a delayed signal trace from the signal trace that has been attenuated by a constant fraction:

$$CFD_{trace}[k] = \sum_{i=1}^{L} \left(F * Trace[k-i] - Trace[k-i-D] \right) \tag{4.5}$$

where D is the delay, L is the length of the running average chosen, and F is the constant fraction. For this work, the CFD trace was computed with a delay of 4 ns, a constant fraction of 0.4, and no running average (L=1). The CFD is a bipolar pulse and the location of its first zero crossing, is used to estimate the arrival time of the original signal. Figure 4-5 shows two event traces, one from the 3x3 EJ309 and one from 5x5 EJ309 and each of their CFDs. Each pulse is assigned a CFD time, and the difference in these times is:

$$\Delta T_{CFD} = CFDTIME_{5x5} - CFDTIME_{3x3} \tag{4.6}$$

where $CFDTIME_{5x5}$ and $CFDTIME_{3x3}$ represent where the 5x5 and 3x3 CFD waveforms, respectively, first cross zero within the 600 ns window shown in Figure 4-3.

Because the Pixie-500 issues triggers in an 8 ns cycle, a pulse may arrive very close to the end of edge of the cycle; consequently one channel may see the pulse in the current 8 ns cycle and be assigned a trigger timestamp, x, while the other channel may see a corresponding pulse in the next cycle and receive a trigger timestamp of x + 1. Consequently, the waveforms are sometimes shifted by one 8 ns cycle. The trigger timestamp, issued by the internal clock, is used to account for these situations by adjusting the CFD extracted time-of-flight, ΔT_{CFD} :

$$TOF_{Adjusted} = \left(\Delta T_{CFD} + (TS_{5x5} - TS_{3x3}) * 8.0ns\right) \tag{4.7}$$

where TS_{5x5} and TS_{3x3} represent the trigger timestamps assigned to each waveform by the internal clock. The time interval between signal arrival times is determined from equation (4.7).

4.3 Time Pick Off Testing

A series of simple experiments were conducted to test the CFD algorithm presented in the previous section. The first experiment used a Tektronix AFG3101 waveform generator, an Ortec DB463 delay box, and the Pixie-500. The waveform generator outputs waveforms at a known frequency with a constant shape and the delay box contains a coil of cable which delays the signal by a user-selected amount before the digitizer analyzes it. The block diagram in Figure 4-4 shows the experiment configuration.

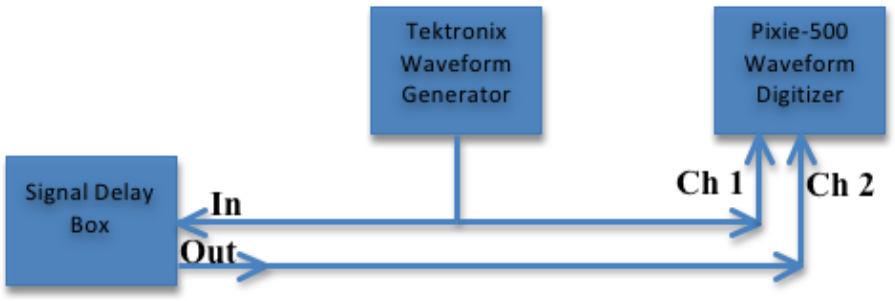

Figure 4-4: Waveform Generator with Delay Box Experiment Configuration

The waveform generator signal was split into two channels; one signal was passed through the delay box with a fixed delay of 12 ns, and the other was sent directly to the digitizer. Each waveform was assigned an arrival time using the CFD algorithm. The distribution of time intervals between each pair of waveforms is shown in Figure 4-5.

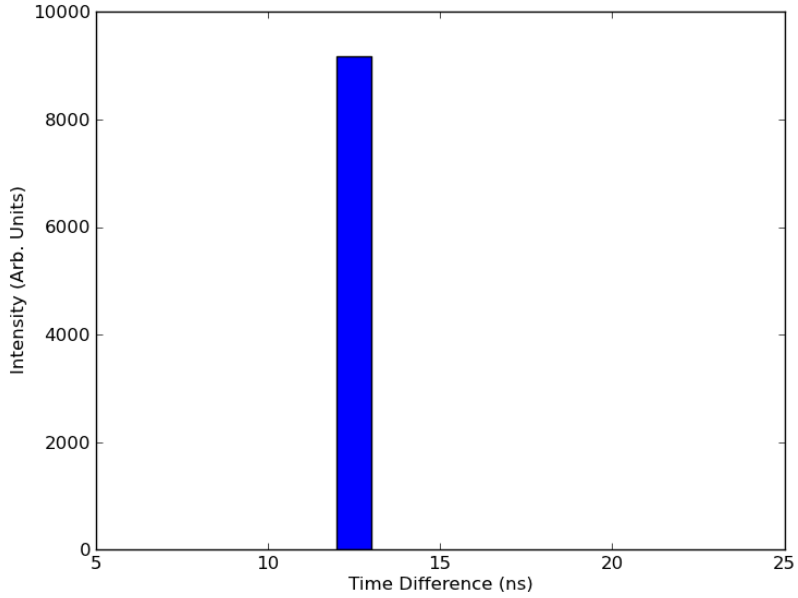

Figure 4-5: Waveform Generator 12 ns Signal Delay

The figure shows that the events had a time interval of approximately 12 ns between them, which indicates the timing algorithm worked as expected given waveforms generated with known shape and frequency.

The CFD algorithm was also tested with random waveform arrival times and a fixed delay using the 5x5 EJ309, a ^{137}Cs source, and the signal delay box. The same experiment configuration shown in Figure 4-6 was implemented, except the 5x5 EJ309 was used in place of the waveform generator. This experiment tested the timing algorithm with waveforms that arrived randomly in time with varying pulse heights. A signal splitter sent the waveform to two channels; one channel was delayed by 12 ns, and the other was sent directly to the digitizer. Figure 4-6 shows the distribution of time intervals between each waveform pair.

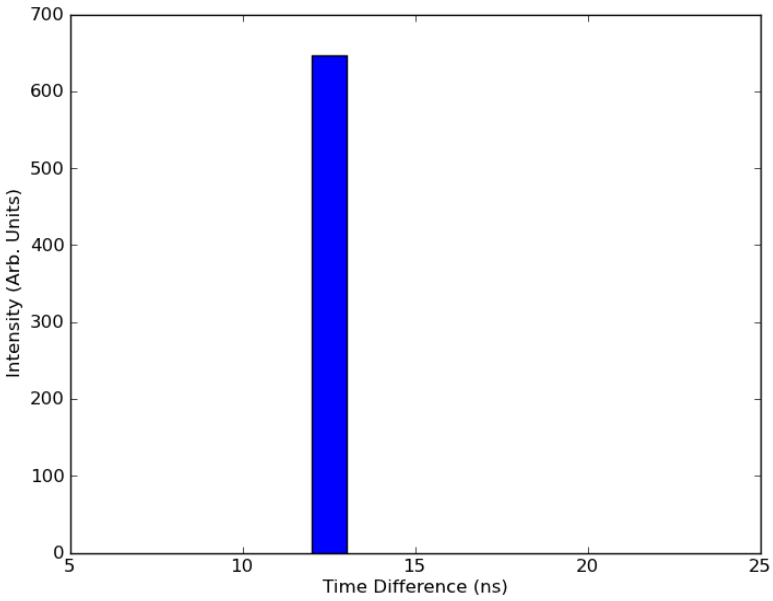

Figure 4-6: Cs137 12 ns Signal Delay

The figure shows the arrival time difference between waveform pairs is approximately 12 ns and that the time pick-off method worked as expected given waveforms with varying amplitudes that were generated randomly by the ^{137}Cs source with a fixed delay.

As the final test of the CFD algorithm, an experiment was conducted which placed a ^{60}Co source between the 5x5 and the 3x3 EJ309 as shown in Figure 4-7 and Figure 4-8.

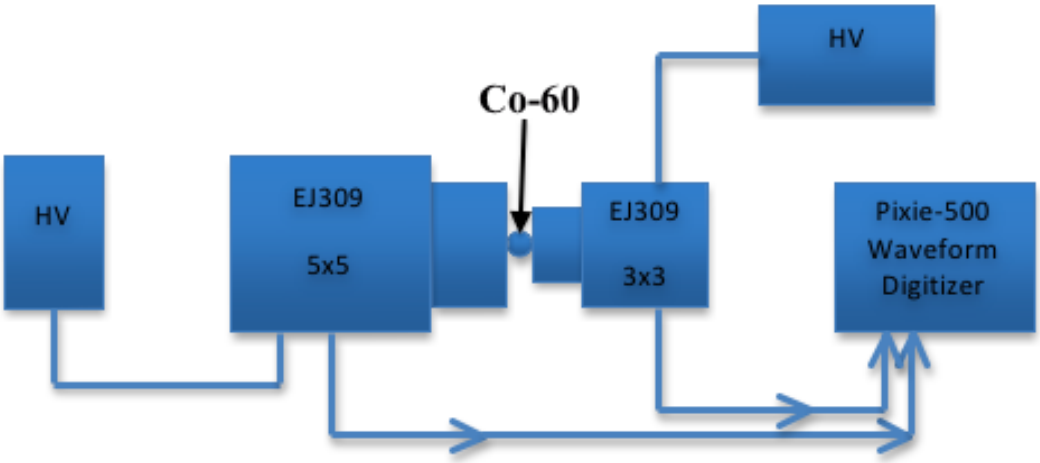

Figure 4-7: ^{60}Co CFD Test Configuration

Figure 4-8: ^{60}Co CFD Test

This experiment added another level of complexity to test the CFD algorithm with; two separate detectors were subjected to coincident gamma radiation, which generates random pulses with varying amplitude. The ^{60}Co source was placed approximately equal distance between the two detectors so that the relative delay between the channels should be approximately zero (equal cable lengths were used). Figure 4-9 shows the distribution of time intervals between each pair of waveforms from the ^{60}Co CFD test.

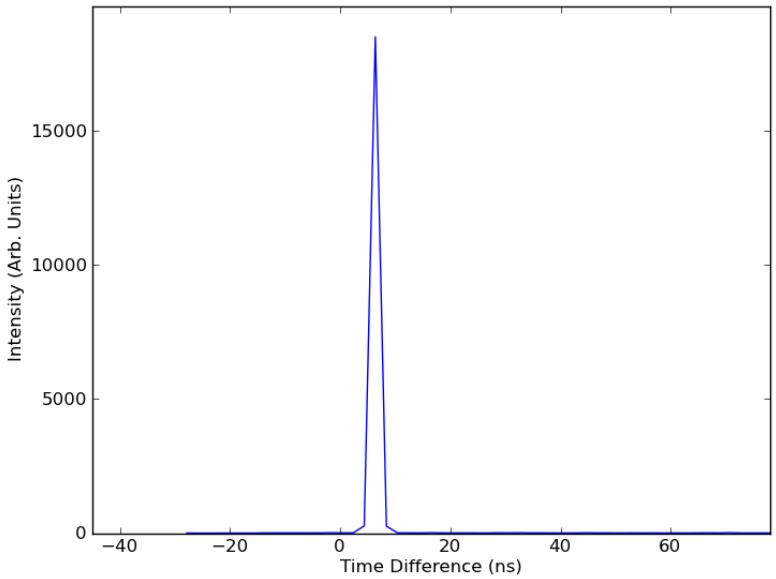

Figure 4-9: ^{60}Co Time Interval Distribution

The figure shows that the majority of the arrival time differences between a waveform pair from the experiment are approximately 6 ns. Given the geometry shown in Figure 4-7, the delay between each channel should be approximately zero; thus the observed difference of approximately 6 ns was most likely due to charge collection time differences between the PMTs of each detector.

It should be noted that the CFD implemented has sub-nanosecond resolution capabilities because it interpolates the CFD trace to find the zero crossing within a given sample [41], but for the purpose of testing the CFD algorithm we used a histogram bin size of approximately 1 ns.

4.4 ^{252}Cf Time-of-Flight Measurement

After establishing the pulse height threshold of 100 keVee, mitigating radio frequency (RF) interference, and testing the time-pick off method, a ^{252}Cf time-of-flight (TOF) experiment was conducted in order to compare the particle classification given by the TOF measurement to the pulse shape discrimination classification. Since gamma rays travel at the speed of light and neutrons travel at a speed dictated by their kinetic energy, it is possible to classify an unknown particle based on the time it takes to travel a fixed distance. Figure 4-10 shows the geometry and layout the ^{252}Cf experiment.

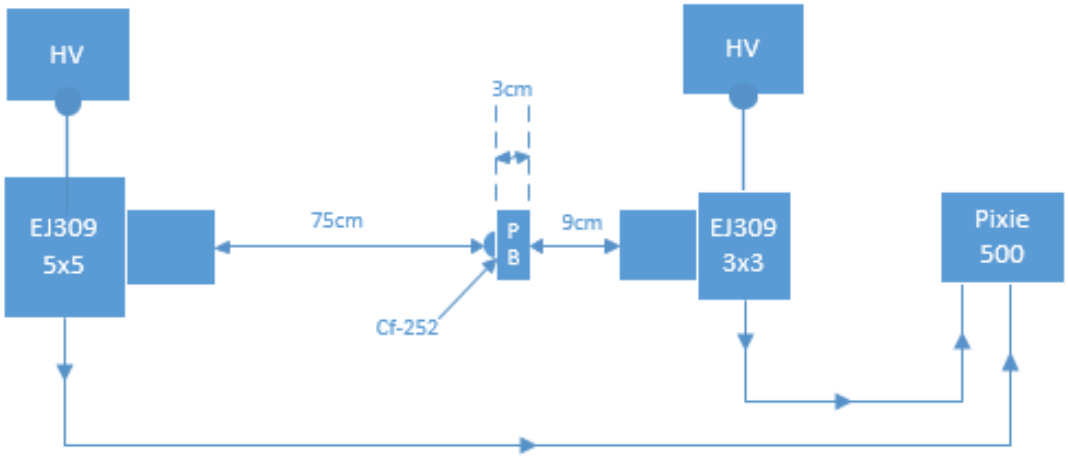

Figure 4-10: ^{252}Cf Time-of-Flight Experiment

A 0.02-µg source ^{252}Cf was placed in front (on the face) of a 3cm thick lead shield to prevent the 3x3 EJ309 from being overwhelmed by gamma rays. The source was placed 12cm from the 3x3 EJ309, and 75cm from the 5x5 EJ309. Figure 4-11 shows a picture of experiment configuration.

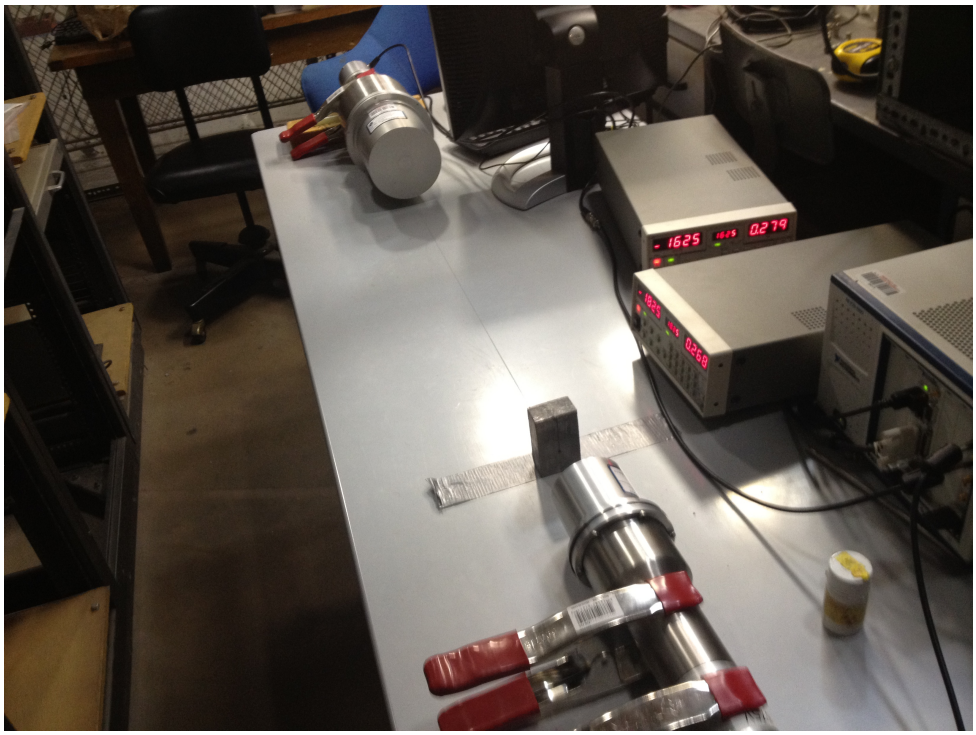

Figure 4-11: ^{252}Cf Experiment Configuration

Following a spontaneous fission event, ^{252}Cf will emit an average of 3.8 prompt neutrons and 7.8 prompt gamma rays. A particle detection and subsequent trigger in the 3x3 served as the "start" time and a detection followed by a trigger in the 5x5 served as the "stop" time. The interval between the start and stop time corresponds to the time of flight of the particle detected in the 5x5. A time-of-flight threshold can then be established; particles with a TOF greater than the established threshold are considered neutrons and particles with a TOF less than the threshold are considered gamma rays.

To conduct the time-of-flight experiment, the Pixie-500 was set to operate in coincidence mode so that a trigger in the "start" detector caused the digitizer to record waveforms in both the 3x3 and 5x5 for a 600 ns time period. A 176 ns coincidence window was used to minimize the number of accidental coincidences.

Using the geometry shown in Figure 4-10, a 30 minute data collection run was taken in the Faraday cage and the results were analyzed using the time pick off method previously described to accumulate the ^{252}Cf TOF histogram shown in Figure 4-12.

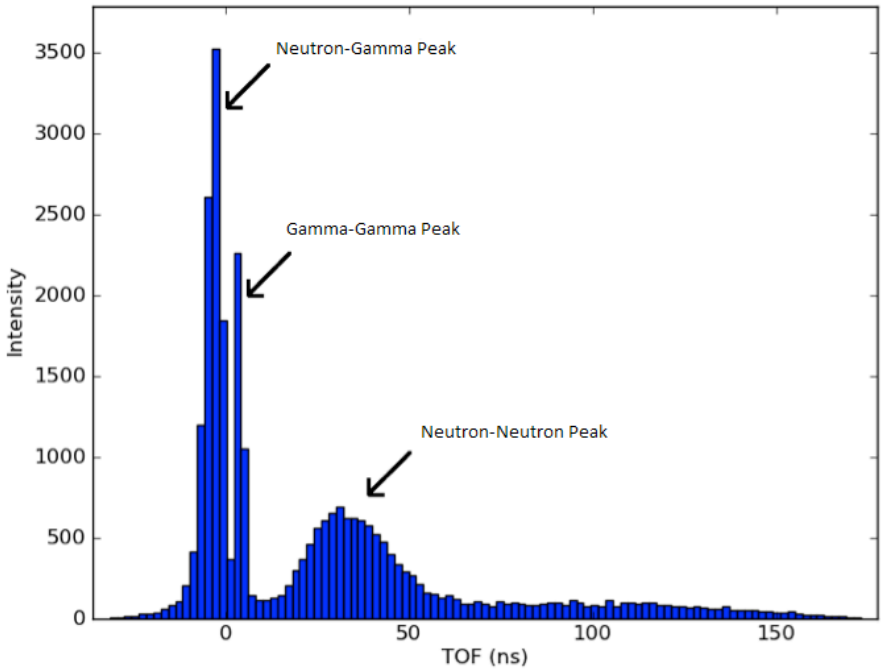

Figure 4-12: ^{252}Cf Time-of-Flight Histogram

The histogram has been adjusted for the PMT charge collection time differences previously shown. The figure shows the three primary peaks that occur in the histogram; there is also an additional peak that is obscured by the "neutron-neutron" peak. Each peak occurs because of a specific sequence of detection. Although the CFD is capable of sub-nanosecond resolution, a bin width of 2 ns was chosen so that the peaks would exhibit a smoother form when compared to a histogram with finer binning. For each spontaneous

fission event, there are four particle detection sequences that can occur. These sequences and their corresponding time of flight ranges are shown in Table 4-1.

Table 4-1: Event Detection Sequences

Detector	3x3 "Start"	5x5 "Stop"	TOF Range (ns)
Particle	Neutron	Gamma	-6.6-0.02
	Gamma	Gamma	2.1-2.2
	Neutron	Neutron	13.1-54.3
	Gamma	Neutron	15.2-56.2

The first peak on the left in Figure 4-12 is the "neutron-gamma" peak, which occurs due to the detection of a neutron in the 3x3 and a gamma ray in the 5x5. The time it takes the neutron to travel the 12 cm between the source and the 3x3 will vary based on its kinetic energy, but the flight time of the gamma ray to the 5x5 will remain constant. Assuming an upper neutron kinetic energy of 12 MeV, with a lower detection threshold of 900 keV, the range of flight times for a neutron to travel 12cm can be determined by using equations (4.8) and (4.9).

$$V_{\text{neutron}} = \sqrt{\frac{E_n}{0.5165}} \tag{4.8}$$

$$T = \frac{D}{V} \tag{4.9}$$

where the speed of the particle, V, is given in cm/ns, E_n is the kinetic energy of the neutron in MeV, D is the distance between the source and the 3x3 in centimeters, and T is the flight time in ns. It was determined that a neutron's flight time to travel 12cm could vary between 2.48 ns for a 12 MeV neutron and 9.1 ns for a 900 keV neutron. Assuming a constant gamma ray speed of 30 cm/ns, the flight time to travel 75cm from the source to the 5x5 is 2.5

ns. Since the TOF of the particle detected in the 5x5 is essentially calculated as the difference in flight times for each particle, the range of TOFs for this scenario should span from -6.6 ns to 0.02 ns. The lower bound represents when a gamma ray triggers in the 5x5 approximately 6.6 ns prior to a 900 keV neutron triggering in the 3x3, and the upper bound represents when a 12 MeV neutron triggers in the 3x3 0.02 ns prior to the gamma ray triggering in the 5x5. The "neutron-gamma" peak shown in Figure 4-12 is only slightly wider than the theoretical range of TOFs, this is probably due to accidental coincidences and timing resolution limitations.

The second peak shown in Figure 4-12 is the "gamma-gamma" peak. This peak represents gamma detections in both the 3x3 and 5x5. Using a gamma speed of 30 cm/ns, the experiment geometry shown in Figure 4-3, and equation (4.9), the flight time for a gamma ray to travel from the source to the 3x3 is 0.4 ns, assuming it was not scattered by the lead. Since the flight time for a gamma to travel to the 5x5 is 2.5 ns, the gamma-gamma peak should occur at approximately 2.1 ns as shown in Figure 4-12 and Table 4-1.

The third and final peak shown is the "neutron-neutron" peak, which corresponds to a neutron detection in the 3x3 and neutron detection in the 5x5; it is shown in Figure 4-13.

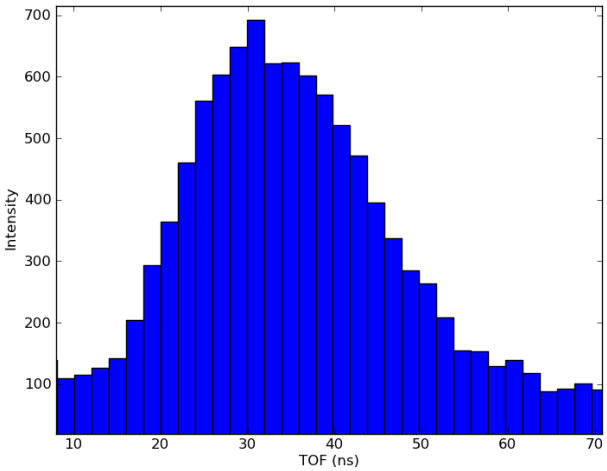

Figure 4-13: Neutron-Neutron/Gamma-Neutron Time-of-Flight Peak

The flight time for a neutron with an energy range from 900 keV to 12 MeV to travel to the 3x3 will vary between 9.1 ns to 2.48 ns, respectively, and for the same energy range, it will vary from 15.56 ns to 56.56 ns to travel 75 cm to the 5x5. This results in a minimum TOF for these events of 13 ns to a maximum TOF of approximately 54 ns, as shown in Table 4-1. This range results in a neutron-neutron peak that should span from approximately 13 ns to 54 ns and have a width of 41 ns.

While the majority of occurrences in this peak represent a neutron detection in the 3x3 and a neutron detection in the 5x5, this sequence does not make up 100% of the events found within the peak. A pair of gamma rays that didn't originate from the same spontaneous fission event can cause a gamma ray to be tagged with a non-physical time-of-flight. This phenomenon occurs because the time-of-flight measurement is based on the time interval between a trigger in the 3x3 and a trigger in the 5x5 but does not consider the origin of either particle. As a result, a particle can trigger in the 3x3 up to 176 ns, (the width of the coincidence window), prior to a different particle triggering in the 5x5. This means that it is possible to tag a gamma ray with a non-physical time-of-flight as large as the coincidence window, and these events are responsible for a portion of the tail of the neutron-neutron peak shown in Figure 4-12 and Figure 4-13. The tail of this peak also consists of particles that may have scattered off the ground, which would increase their time of flight due to a lengthened flight path. These scattering events are probably mostly responsible for the accumulation of the tail of the neutron-neutron peak.

Table 4-1 also refers to a "gamma-neutron" pair of events, which represents a gamma interaction in the 3x3 and a neutron interaction in the 5x5. These coincidences are hidden underneath the neutron-neutron peak shown in Figure 4-12 and represent only a small fraction of events because of the low count rate of gamma-neutron coincidences. The flight time for a gamma ray to travel to the 3x3 (assuming no scattering by the lead block) is approximately 0.4 ns. The flight time for a neutron with an energy range of 12 MeV to 900 keV to travel to the 5x5 ranges from approximately 15.56 ns to 56.56 ns, respectively. Consequently, the gamma-neutron peak should span from 15.16 ns to 56.16 ns as shown in Table 4-1, but the lead block used to keep the trigger detector from being over-whelmed with

counts scattered most of the gamma rays that would otherwise be triggers in the 3x3. Consequently, the broad gamma-neutron peak is low in amplitude and is hidden by the neutron-neutron peak.

A MCNPX-PoliMi simulation of the TOF experiment was run in order to compare the simulation results to the experiment outcome [42]. Figure 4-14 shows the model used to simulate the experiment.

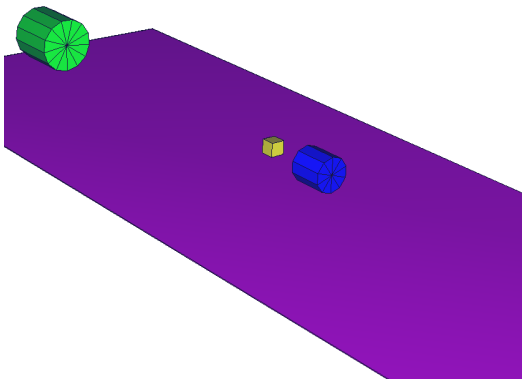

Figure 4-14: MCNP TOF Experiment Model

For simulation purposes, the tabletop, both scintillator volumes, and the 3cm thick lead block were modeled as shown in the figure. Figure 4-15 shows the results of the simulation.

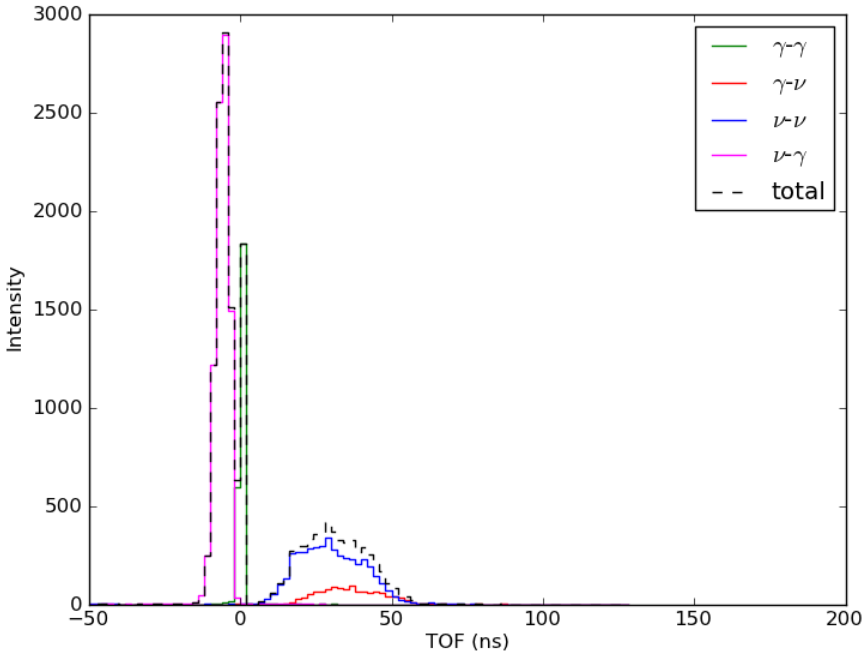

Figure 4-15: MCNP TOF Experiment Simulation

The simulation shows good agreement with the TOF experiment and indicates that the gamma-neutron peak is in fact hidden beneath the neutron-neutron peak.

The TOF threshold was set to be the point at which the "neutron-neutron" peak began. Figure 4-12 and Figure 4-13 show the peak starting to rise around 12 ns; therefore, the TOF measurement tagged particles with a time-of-flight greater than 12 ns as a neutron and particles with a time-of-flight less than 12 ns (but greater than 0) as a gamma ray.

Three separate methods of PSD were performed on the set of waveforms from the 5x5. In this way it was possible to classify a particle based on its time-of-flight and compare that classification to the pulse shape analysis results.

4.5 Digital Charge Integration

The first PSD method investigated was the digital charge integration technique. The charge integration technique relies on the fact that heavy charged particles produce a greater fraction of light during the decay of the pulse than recoil electrons do. This causes the tail area of a neutron pulse to typically represent a larger fraction of the total area under the waveform when compared to the tail area of a waveform caused by a gamma ray. Figure 4-16 shows a typical waveform that was analyzed with the digital charge integration algorithm.

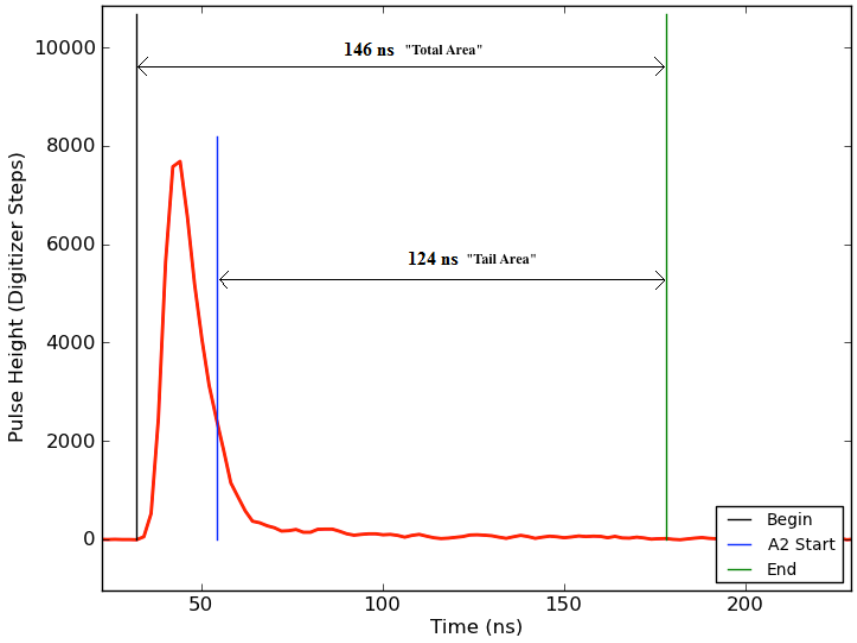

Figure 4-16: Description of the Area Ratio for a Typical Waveform

For each waveform analyzed, the beginning and the end of the pulse were marked when the leading and trailing edge rose and fell below an amplitude threshold. The threshold was

established by determining where the moving average of the waveform rose above or fell below the RMS level of the waveform. The tail area, A_{Tail}, is taken to start 10 ns beyond the location of the peak since this region exhibits the most shape difference for a gamma and a neutron event. For the waveform shown in Figure 4-16, the beginning of the pulse was marked at 32 ns and the end was marked at 178 ns, for a total width of 146 ns. The tail-to-total area ratio is the parameter that the digital charge integration algorithm uses to classify each particle:

$$R = \frac{A_{Tail}}{A_{Total}} \tag{4.10}$$

The area under the pulse, from beginning mark to the end mark in Figure 4-16, represents A_{Total} in equation (4.10). The start of the tail area region in Figure 4-16 is marked at 54 ns and the tail region extends to the end of the pulse. Using A_{Total} and A_{Tail}, equation (4.10) can be evaluated to find the area ratio parameter, R, and a particle classification can be made.

This process was repeated for each waveform that was analyzed. Figure 4-17 shows a scatter plot of the calculated area ratio versus the pulse height for each waveform.

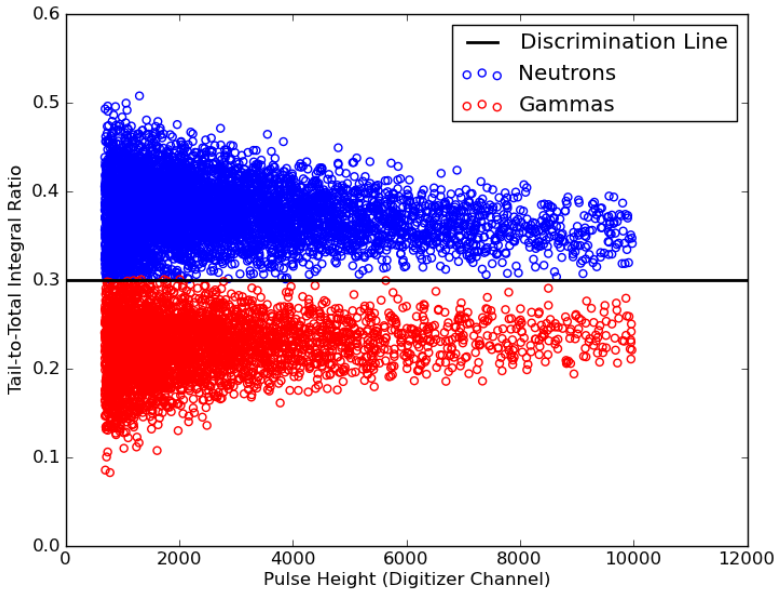

Figure 4-17: Area Ratio vs. Pulse Height

Using this figure, an area ratio threshold of 0.3 was selected so that the PSD algorithm classified waveforms with an area ratio greater than 0.3 as neutrons and waveforms with an area ratio less than 0.3 as gamma rays. Figure 4-18 shows a scatter plot of the tail area versus the total area for each waveform.

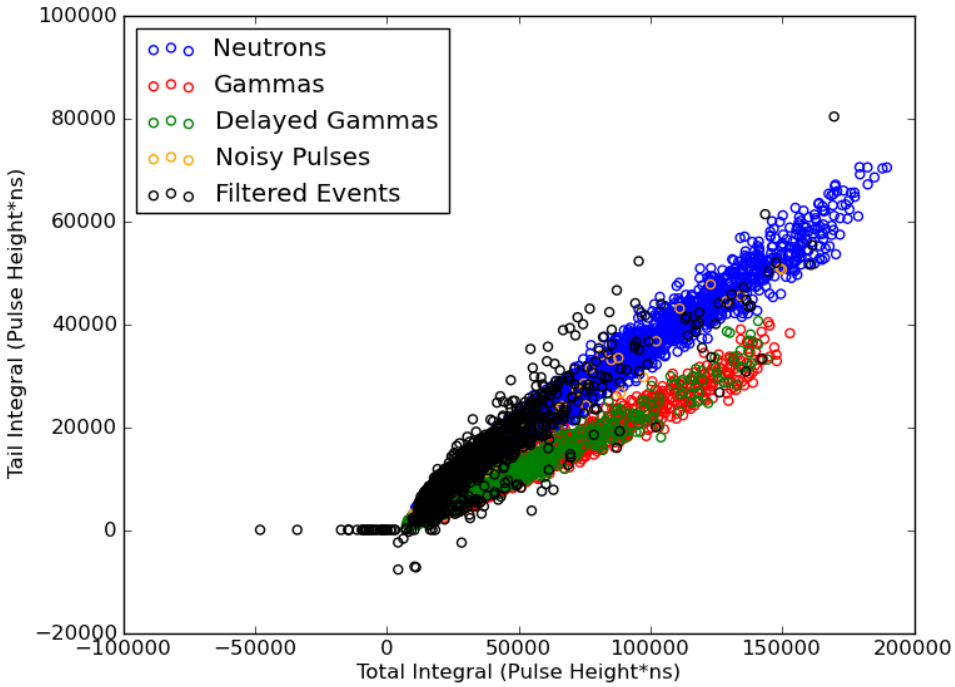

Figure 4-18: Digital Charge Integration PSD

The figure above shows the digital charge integration results in terms of four specific categories and an additional 'Filtered Events' category.

The filtered events were identified using a data-cleaning algorithm that checked for double pulsing and other anomalous waveforms that could cause misleading pulse shape analysis. In addition to the minimum pulse height requirement, the maximum amplitude of each waveform was required to occur at least 20 ns into the recording window to ensure that the CFD would properly locate the peak. Once the peak was located, the recording window was scanned to ensure that there were no other pulses later in time by requiring the leading edge to remain below 30% of the pulse height threshold. Each waveform that passed these requirements was also subject to a maximum rise time requirement of 12 ns. The rise time was noted as the time interval between where the leading edge first rose above the "start"

threshold, described previously, and location of the maximum amplitude in the recording window. This requirement was established to ensure there were no anomalous waveform shapes on the leading edge, such as a double pulse, and also to ensure there were no pulses prior to a pulse that exhibited the maximum amplitude in the recording window.

Each waveform that passed the data-cleaning requirements was sorted into the four additional categories based on its area ratio and time-of-flight. The TOF measurement tagged particles with a time-of-flight greater than 12 ns as neutrons; however, this method is not 100% accurate due to delayed gammas that are emitted from spontaneous fission of ^{252}Cf. Using both the tail-to-total area ratio and the time of flight for each particle, it is possible to classify them as 'neutrons', 'gammas', 'delayed gammas', or 'noisy pulses', as shown in Figure 4-18. Table 4-2 shows the requirements for a specific particle classification.

Table 4-2: Charge Integration Particle Classification Requirements

Classification	Area Ratio	TOF (ns)
Neutron	> 0.3	> 12
Gamma	< 0.3	< 12
Delayed Gamma	< 0.3	> 12
Noisy Pulse	> 0.3	< 12

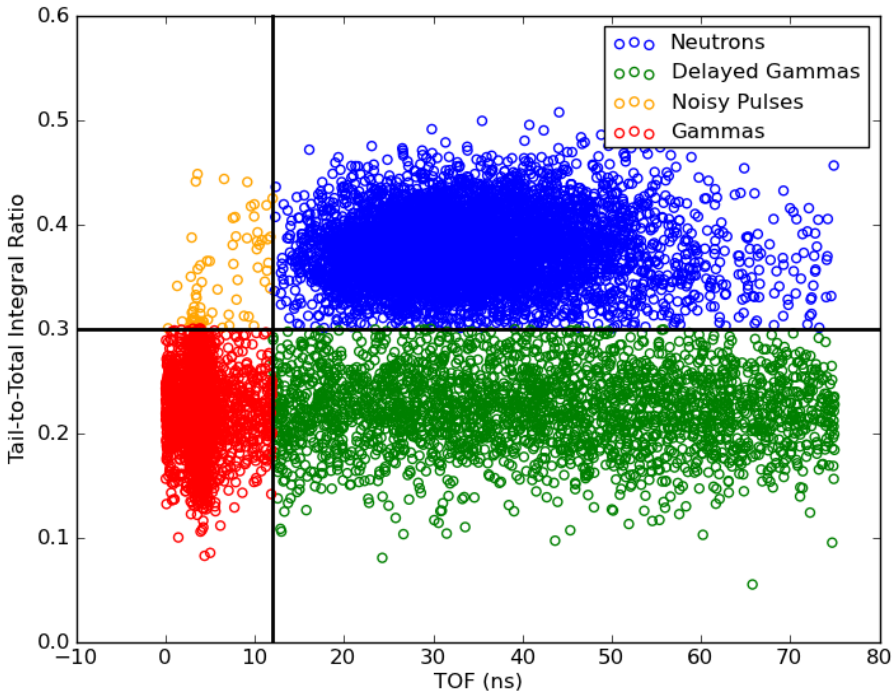

Figure 4-19: Area Ratio vs. Time-of-Flight

Figure 4-19 shows the division of the particle classification categories that are based on area ratio and TOF. Table 4-2 indicates that a particle is classified as a 'noisy pulse' if the TOF measurement and the charge integration are inconsistent. An area ratio greater than 0.3 indicates the particle should be a neutron but a time-of-flight less than 12 ns suggests the particle is a gamma ray. These pulses could be a result of several alternative processes and it is difficult to say for certain which classification they should receive. An example of a 'noisy' pulse is shown in Figure 4-20.

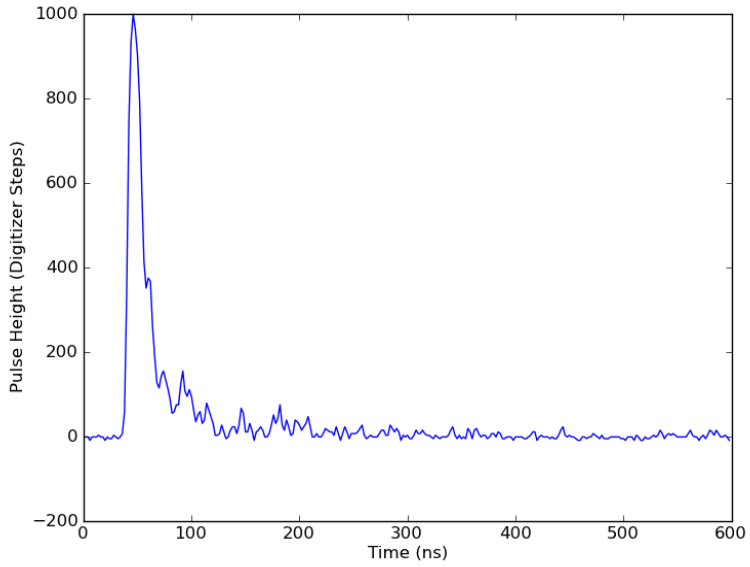

Figure 4-20: A Typical 'Noisy Pulse'

In this case, the excess noise on the tail of the pulse resulted in a pulse shape parameter (R > 0.3) that is inconsistent with the particle's time-of-flight (TOF < 12ns). Basic kinetics equations (Eq. 4.8 and 4.9) can be used to show that a particle with a flight time of less than 12 ns to travel from the source to the 5x5 (75cm) is most likely a gamma ray since this would require a neutron energy of approximately 20 MeV. The neutron emission spectrum from ^{252}Cf exhibits very few neutrons emitted which have an energy greater than 12 MeV, so it is assumed that most particles with a TOF of less than 12 ns are in fact gamma rays [43]. A few of these waveforms could also be accidental neutron coincidences which occur when a neutron from an unrelated spontaneous fission event triggers in the 5x5 immediately after a trigger is registered in the 3x3 from a particle originating from a different spontaneous fission event.

After examining several of the waveforms in the 'noisy pulse' category, it was determined that some of these waveforms should have been filtered out as a "bad waveform" due to double pulsing and other waveform anomalies. The 'noisy pulse' classification will

be made in the PSD methods that follow as well; similarly, it is made when the time of flight measurement and the pulse shape analysis do not agree, and it is typically caused by noise on the pulse or due to a misshaped waveform that should have been filtered out. These results are relatively inconsequential due to the low number of 'noisy pulse' classifications that were made, which typically accounted for less than 1 % of the total number of accepted pulses. Figure 4-21 shows the tail-to-total area scatter plot after the anomalous waveforms (shown in black in Figure 4-18) were filtered out.

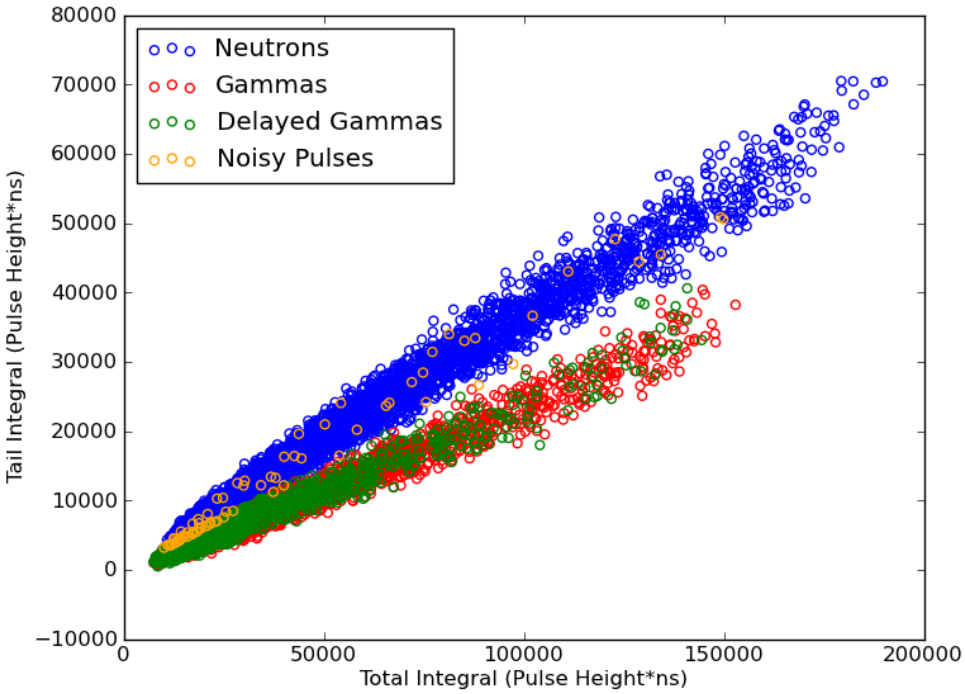

Figure 4-21: Digital Charge Integration PSD (No Filtered Events)

This figure indicates that all the delayed gamma ray events fall within the gamma region of the scatter plot and that most of the 'noisy pulses' fall between the gamma and neutron region. Table 4-3 quantifies the results shown in Figure 4-21.

Table 4-3: Digital Charge Integration Results

Classification	Occurrence	% of Total
Neutron	5778	46.99
Gamma	3831	31.16
Delayed Gamma	2607	21.20
Noisy Pulse	78	0.65

The table shows that most particles were classified as neutrons but that the total gamma ray classifications (including both gamma and delayed gamma) outnumbered the neutron classifications. A scatter plot of the tail area versus the total area that includes only particles classified as a neutron or gamma ray (including 'delayed gammas') is shown in Figure 4-22.

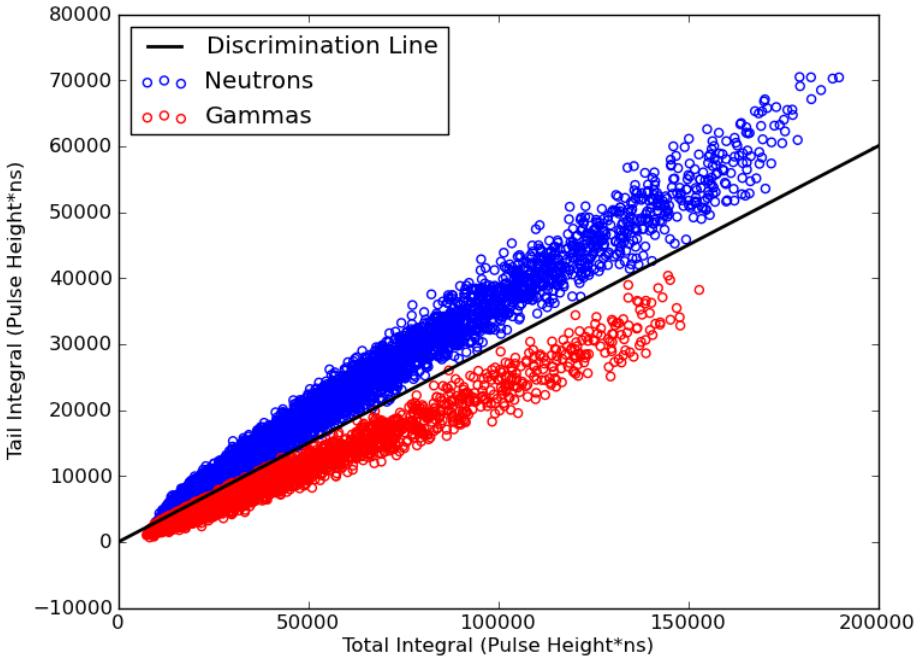

Figure 4-22: Digital Charge Integration PSD (Neutrons and Gammas)

The scatter plot displays the clear separation obtained by the digital charge integration method. As the neutron energy decreases, however, the discrimination is less clear. Figure 4-23 shows the region where the neutrons have much lower energy.

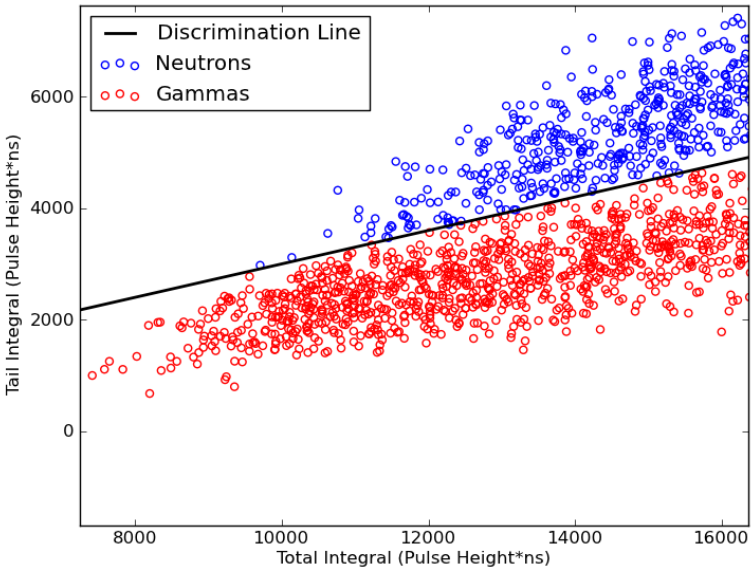

Figure 4-23: Low Energy Region

The separation made by the discrimination line in the low energy region is much less distinguishable than it is at higher energy regions, shown in the upper right quadrant of Figure 4-22.

4.6 Pattern Recognition Method

The next method of digital pulse shape discrimination investigated was a pattern recognition technique. The pattern recognition method compares a known reference waveform with each waveform in question by treating each as a vector and computing the scalar product between the reference and the "unknown" pulse. D. Takaku and T. Oishi have previously shown a similar method to exhibit adequate pulse shape discrimination results. In this work, the reference vector was chosen to be a waveform caused by a gamma interaction in the EJ309. A gamma waveform was chosen as the reference vector because the pulse shape remains fairly constant and is independent of energy. Waveforms were collected from a ^{60}Co source and saved to construct an average gamma waveform, which was regarded as the reference vector for this analysis. The reference waveform is shown below in Figure 4-24.

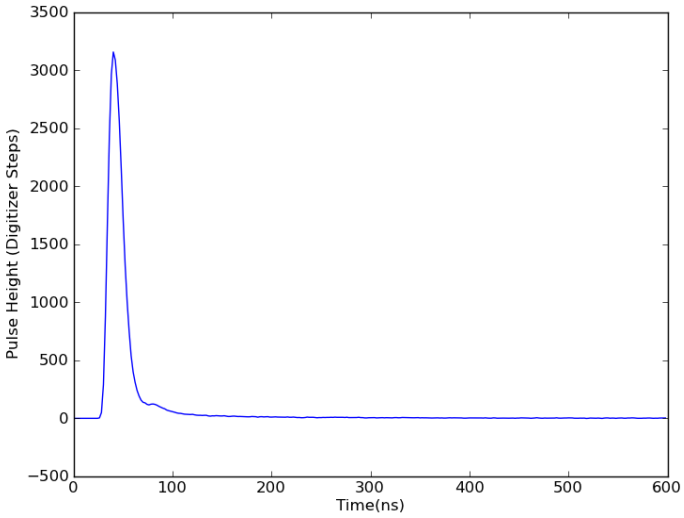

Figure 4-24: Pattern Recognition Reference Waveform

The figure shows that the reference waveform exhibits very little noise or fluctuation about the baseline, this is a result of averaging over many waveforms collected during the ^{60}Co experiment. In an attempt to fairly compare the reference waveform, which exhibits little noise, to a waveform in question, each waveform's "tail" region was passed through a 5 point smoothing function, given by equation (4.11), in an attempt to filter out statistical amplitude fluctuations on the tail caused by noise:

$$x_i = \frac{1}{5}\left(x_{i-2} + x_{i-1} + x_i + x_{i+1} + x_{i+2}\right) \qquad (4.11)$$

The resulting smoothed tail section was regarded as a vector, X_{tail}, whose components are the digitized amplitude, x_i, at the corresponding sampling time. Taking the scalar product of the waveform's smoothed tail, vector X_{tail}, and the tail of the reference waveform, vector Y_{tail}, is the basis of which the pulse shape discrimination was performed. The scalar product is given by:

$$X_{Tail} \cdot Y_{Tail} = \sum_i x_i y_i \qquad (4.12)$$

Figure 4-25 shows a typical pattern recognition comparison.

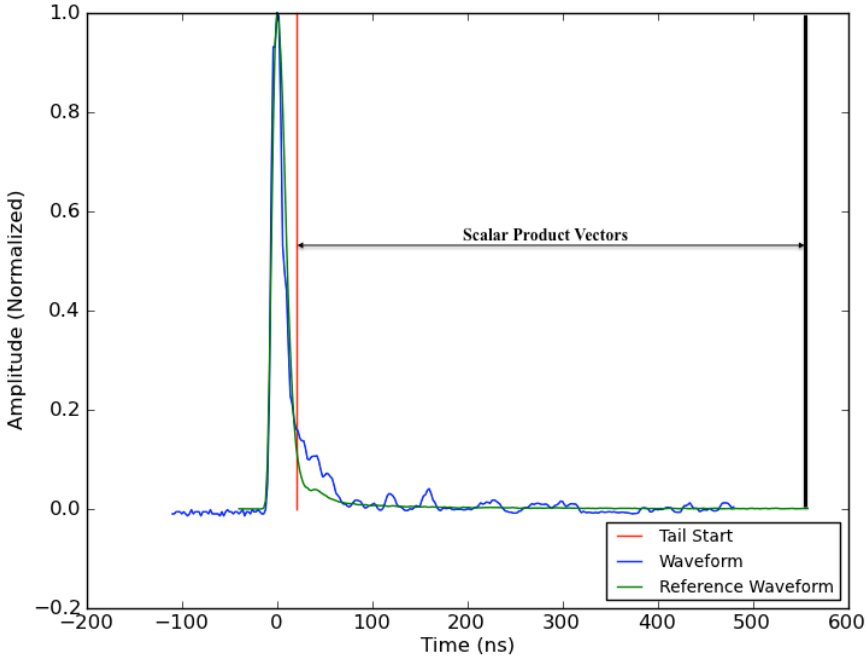

Figure 4-25: Sample Waveform vs. Reference Waveform

The ratio, R, between the scalar product of the tails and the product of the magnitudes of each vector is the pulse shape parameter for this analysis:

$$R = \frac{X_{Tail} \cdot Y_{Tail}}{||X||||Y||} \tag{4.13}$$

where $X_{Tail} \cdot Y_{Tail}$ is the scalar product of the two tail vectors, and $||X||$ and $||Y||$ are the magnitudes of each waveform, respectively. It should be noted that the magnitudes represent the magnitude of the entire waveform and are given by:

$$||X|| = \sqrt{\sum_{Length} x_i^2} \tag{4.14}$$

$$||Y|| = \sqrt{\sum_{Length} y_i^2} \tag{4.15}$$

Figure 4-25 shows that the tail was taken to start at a fixed point of 20 ns beyond the peak of the waveform so that the scalar product is computed only where the shape difference of a typical neutron and gamma waveform is enhanced. Given the scalar product of the tails and the magnitudes of each waveform, the pulse shape parameter, R, can be obtained.

This process was repeated for each waveform analyzed, and a scatter plot of the pulse shape parameter versus the pulse height for each pulse is shown in Figure 4-26.

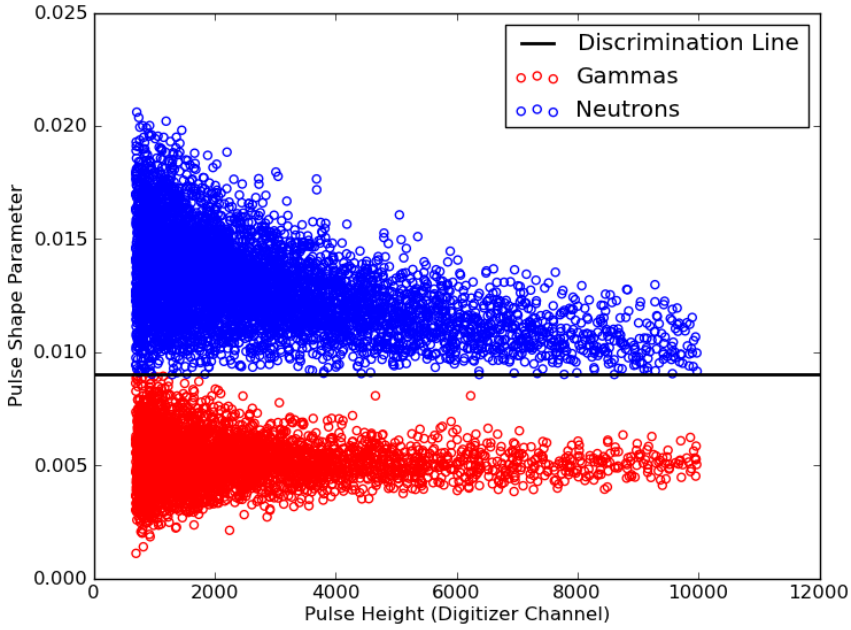

Figure 4-26: Scalar Product Ratio vs. Pulse Height

The span of calculated pulse shape parameters ranges from approximately 0.001 to 0.021 where values closer to zero indicate a pulse shape that is similar to the reference waveform shape.

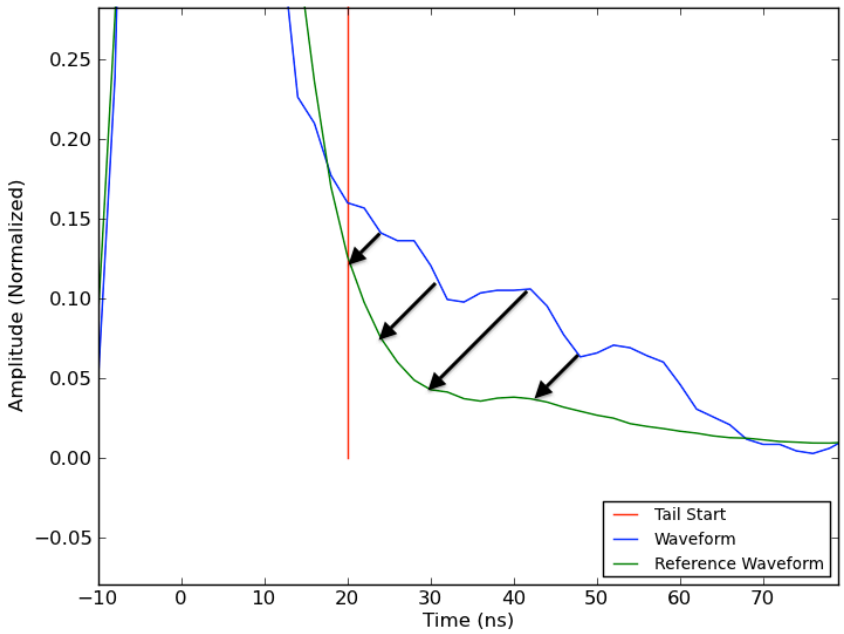

Figure 4-27: Reference Waveform vs. Sample Waveform

Figure 4-27 shows that as the sample waveform in question becomes more similar in shape to the reference waveform, the components of the sample waveform tail become smaller in magnitude sooner in time. This leads to a smaller scalar product and a pulse shape parameter closer to 0. Using the logic just described and Figure 4-26, a discrimination point of R = 0.009 was chosen so that the PSD algorithm classified particles with a pulse shape parameter greater than 0.009 as a neutron and particles with a pulse shape parameter less than 0.009 as a gamma ray.

The time-of-flight measurement was used in order to further categorize the pulses in a manner similar to which was previously shown in the charge integration PSD method. The pulses were categorized based on their time-of-flight and their pulse shape parameter, R. The requirements for a specific particle classification are shown in Table 4-4.

Table 4-4: Pattern Recognition Particle Classification Requirements

Classification	R	TOF (ns)
Neutron	> 0.009	> 12
Gamma	< 0.009	< 12
Delayed Gamma	< 0.009	> 12
Noisy Pulse	> 0.009	< 12

Figure 4-28 shows a scatter plot of the pulse shape parameter versus the TOF for each particle and the division of the classification regimes shown in Table 4-4.

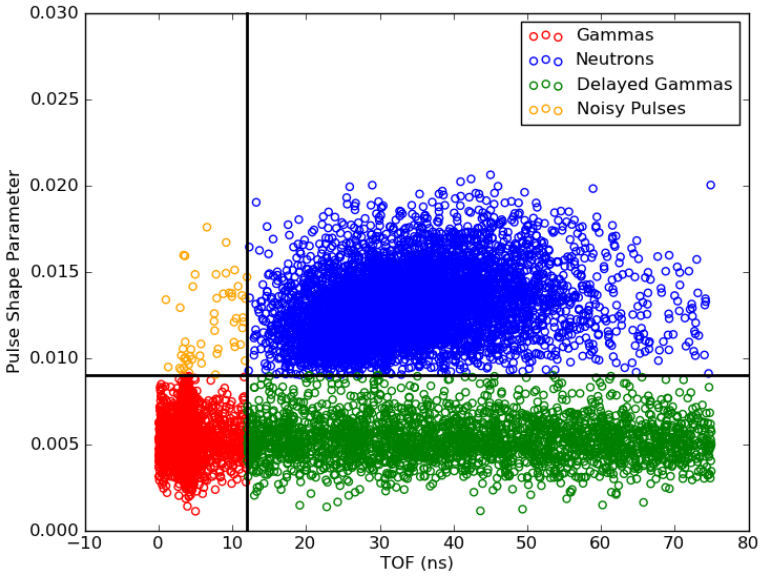

Figure 4-28: Scalar Product Ratio vs. Time-of-Flight

The noisy pulse classification occurs when the time-of-fight measurement and the PSD method do not concur and is similar to the noisy pulse classification shown in the charge integration results. These pulses exhibit large fluctuations on the tail of the pulse that cause the pulse shape parameter to fall within the neutron category, but their time-of-flight classifies them as a gamma ray. For reasons previously discussed, these particles are assumed to be gamma rays and represent only a small fraction of the total classifications made. Table 4-5 quantifies the classification results.

Table 4-5: Pattern Recognition Results

Classification	Occurrence	% of Total
Neutron	5827	47.39
Gamma	3856	31.36
Delayed Gamma	2558	20.80
Noisy Pulse	53	0.43

These results are similar to the charge integration method in that the total number of gamma classifications outnumbers the neutron classifications and that the noisy pulses account for less than one percent of the total.

4.7 Curve Fitting Method

The final method of digital pulse shape discrimination investigated in this work is a curve fitting technique. This method relies on the fact that a neutron pulse will decay slightly slower than a gamma ray pulse due to its increased light output in the tail region of the pulse. Similar to the pattern recognition method, the curve fitting routine was previously shown to exhibit adequate PSD results by D. Takaku and T. Oishi [0]. To carry out the analysis, the tail of each waveform was passed through a 5 point smoothing function shown in equation (4.11) and was fitted with the curve:

$$y = e^{-\lambda t} \tag{4.16}$$

The decay constant, λ, is the pulse shape parameter that is obtained for each waveform. The delayed light output from a neutron interaction in the liquid scintillator causes a neutron pulse to have a decay constant that is slightly smaller than typical gamma ray waveform decay constants. Figure 4-29 and Figure 4-30 show a typical fit for both a gamma ray and a neutron waveform.

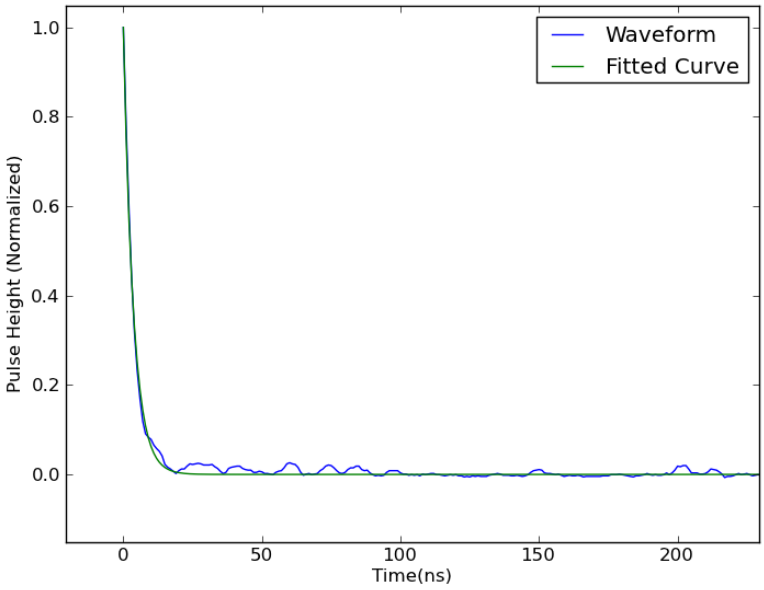

Figure 4-29: A Typical Gamma Waveform Fit

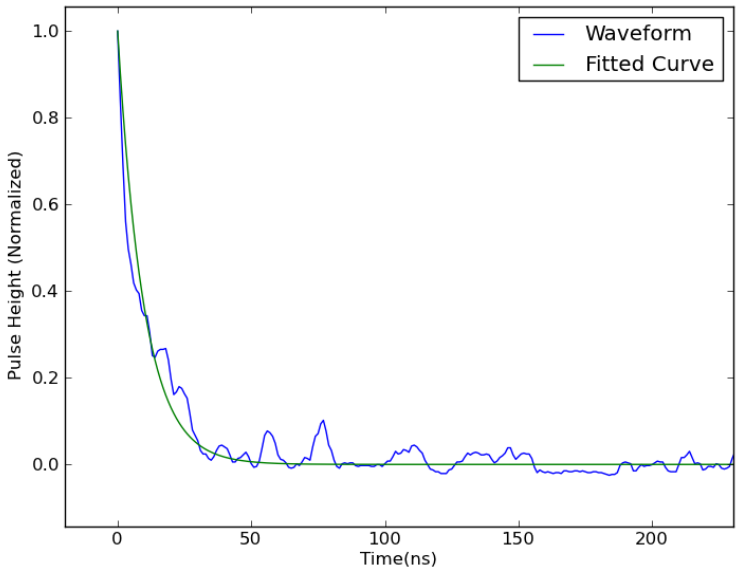

Figure 4-30: A Typical Neutron Waveform Fit

The decay constant for the gamma waveform fit, shown in green in Figure 4-29, is approximately 0.28 while it is approximately 0.1 for the neutron waveform fit shown in Figure 4-30. A scatter plot of the pulse shape parameter, λ, versus the pulse height is shown in Figure 4-31.

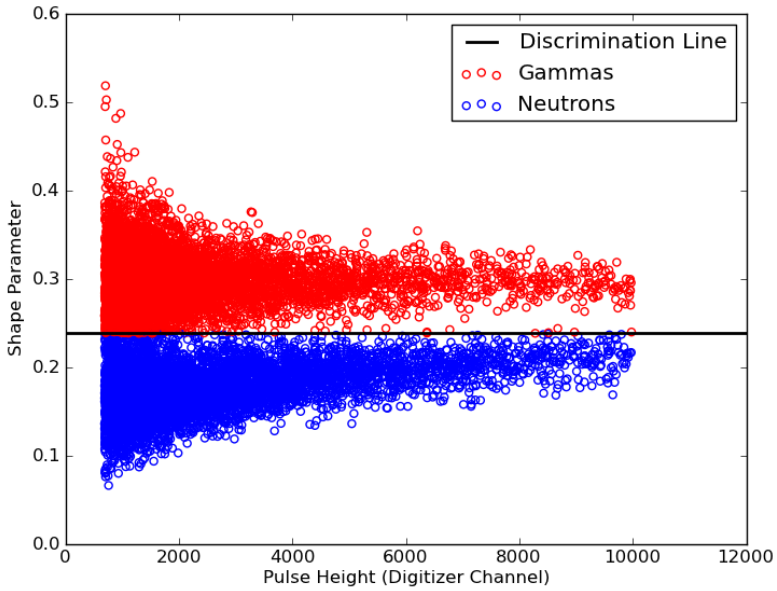

Figure 4-31: Pulse Shape Parameter (λ) vs. Pulse Height

Based on this plot, the PSD algorithm classifies a particle as a neutron if it produces a waveform with a fitted decay constant less than 0.238, and as a gamma ray if the waveform was fit with a decay constant greater than 0.238.

The time-of-flight measurement was used as previously shown to further classify the particles based on their time-of-flight. The requirements for a specific classification are given in Table 4-6.

Table 4-6: Curve Fitting Particle Classification Requirements

Classification	λ	TOF (ns)
Neutron	< 0.238	> 12
Gamma	> 0.238	< 12
Delayed Gamma	> 0.238	> 12
Noisy Pulse	< 0.238	< 12

The classification categories can be seen clearly in the scatter plot of the pulse shape parameter versus the TOF in Figure 4-32.

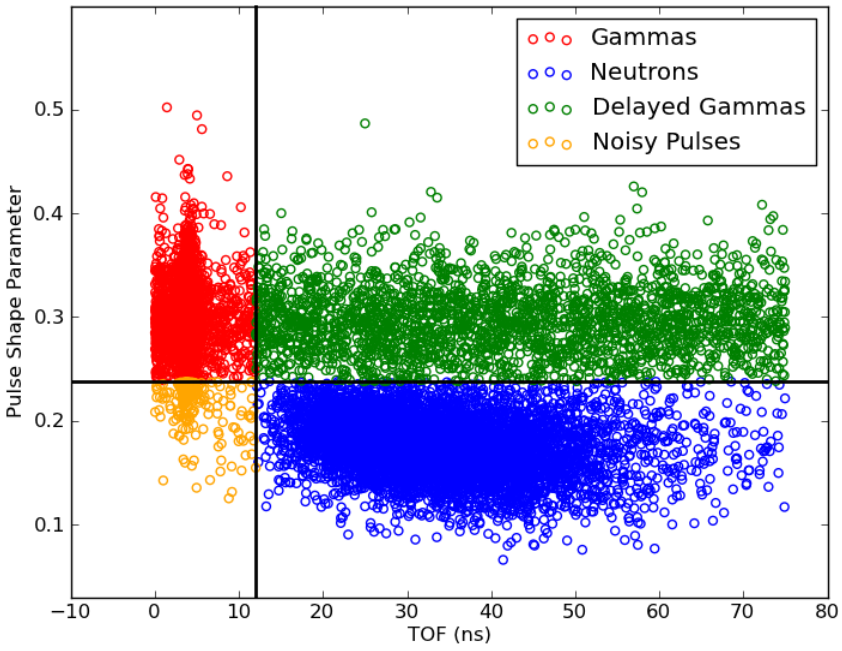

Figure 4-32: Pulse Shape Parameter (λ) vs. Time-of-Flight

The classification results are quantified in Table 4-7, shown below.

Table 4-7: Curve Fitting Results

Classification	Occurrence	% of Total
Neutron	5941	48.32
Gamma	3705	30.13
Delayed Gamma	2444	19.87
Noisy Pulse	204	1.66

The curve fitting pulse shape discrimination results show that the number of neutron, gamma, and delayed gamma classifications are similar to results previously reported using different methods of PSD. The curve fitting method seems to be more sensitive to noise in that the number of noisy pulses accounted for 1.66% of the total, while the other PSD methods resulted in less than 1%.

4.8 PSD Figure-of-Merit

The figure-of-merit (FOM) for a particular PSD method can provide a quantitative degree of the PSD algorithm quality. Typically, the FOM is based on a measure of separation between peaks in a histogram of the calculated pulse shape parameter. In this work, we based our FOM on the particle misclassification rate, which can be obtained by calculating the area of overlap that the two peaks exhibited in the pulse shape parameter histogram. To obtain the overlap area, each peak was fit with a Gaussian distribution given by:

$$G(x) = Ae^{\frac{-(x-\mu)^2}{2\sigma^2}} \tag{4.17}$$

where σ is the standard deviation about the mean, μ, and A is a constant. Figure 4-33 shows the FOM for the digital charge integration method.

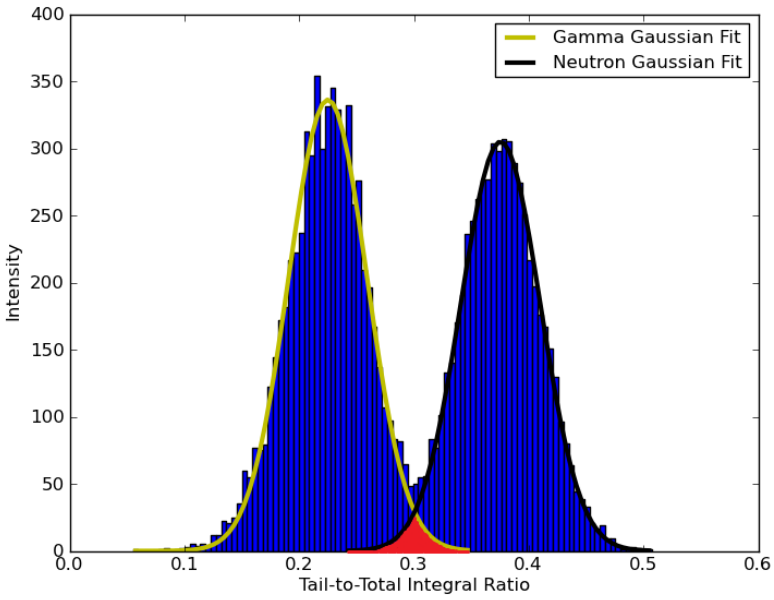

Figure 4-33: Digital Charge Integration Figure of Merit

The figure shows the histogram of pulse shape parameter, the tail-to-total area ratio, with a Gaussian distribution fit to each peak. Table 4-8 shows the fitted parameters and the intersection for the gamma and neutron Gaussian distributions.

Table 4-8: Digital Charge Integration FOM Parameters

Parameter	Gamma Gaussian	Neutron Gaussian
μ	0.224	0.375
σ	0.0342	0.0345
A	336.20	304.93
X_o	0.30	

The intersection point of the gamma and neutron Gaussian distributions shown in the figure was calculated as X_o and the area under the intersection is the estimated particle misclassification rate. The intersection point is the pulse shape parameter at which the neutron and gamma Gaussian distributions are equivalent and can be found by setting the distributions equal to each other and solving for x:

$$A_\gamma e^{\frac{-(x-\mu_\gamma)^2}{2\sigma_\gamma^2}} = A_\nu e^{\frac{-(x-\mu_\nu)^2}{2\sigma_\nu^2}} \tag{4.18}$$

where subscripts γ and ν represent the parameters for the gamma and neutron Gaussian distributions, respectively. Solving for x gives two unique solutions:

$$x = \frac{1}{\sigma_\gamma^2 - \sigma_\nu^2}\left(\pm\sqrt{-\sigma_\gamma^2\sigma_\nu^2\left(2\ln\left(\frac{A_\gamma}{A_\nu}\right)\sigma_\gamma^2 - 2\ln\left(\frac{A_\gamma}{A_\nu}\right)\sigma_\nu^2 - \mu_\gamma^2 + 2\mu_\gamma\mu_\nu - \mu_\nu^2\right)} + \sigma_\gamma^2\mu_\nu - \sigma_\nu^2\mu_\gamma \right) \tag{4.19}$$

where the most appropriate solution can be chosen from the pulse shape parameter histogram. The misclassification rate can then be given by equation (4.20).

$$\frac{\int_{-\infty}^{X_0} G_v(x)\,dx + \int_{X_0}^{\infty} G_\gamma(x)\,dx}{\int_{-\infty}^{\infty} \left(G_v(x) + G_\gamma(x)\right)dx} \tag{4.20}$$

The red shaded area in Figure 4-33 represents particle misclassification given by equation (4.20); it was determined that the digital charge integration method misclassified approximately 1.41% of the particles that were analyzed.

The figure-of-merit for the pattern recognition method is shown below in Figure 4-34.

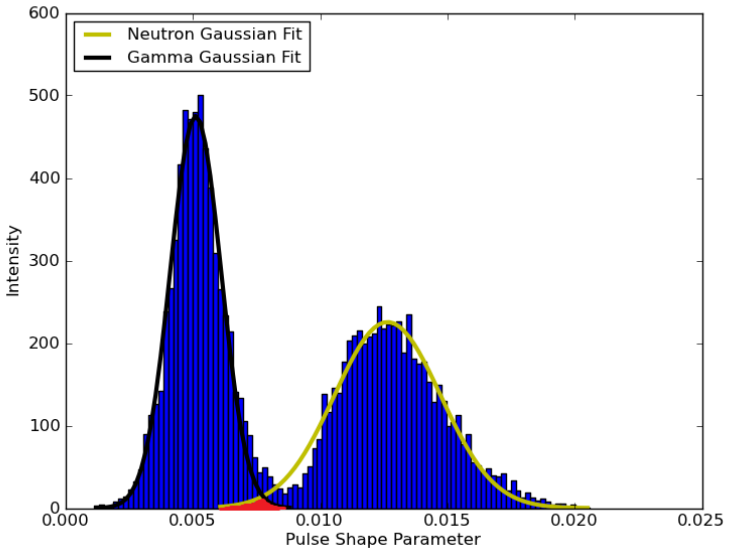

Figure 4-34: Pattern Recognition Figure-of-Merit

The pattern recognition figure-of-merit shows that the Gaussian fit represents the gamma peak well, but the neutron Gaussian fit is less representative of the experimental data due to

the slight asymmetry shown in the neutron peak. The best-fit parameters for each peak and the intersection of the distributions are shown in Table 4-9.

Table 4-9: Pattern Recognition Figure-of-Merit Parameters

Parameter	Gamma Gaussian	Neutron Gaussian
μ	0.005	0.0126
σ	0.0009	0.002
A	475.23	225.40
X_o	0.0777	

Evaluating equation (4.20) with the appropriate bounds and parameters for each distribution yields a misclassification of 0.67% of the waveforms analyzed according to this figure-of-merit. This result may be slightly misrepresentative of the true situation since the neutron Gaussian distribution doesn't fit well with the tail of neutron peak.

The figure-of-merit for the curve fitting routine is shown below in Figure 4-35.

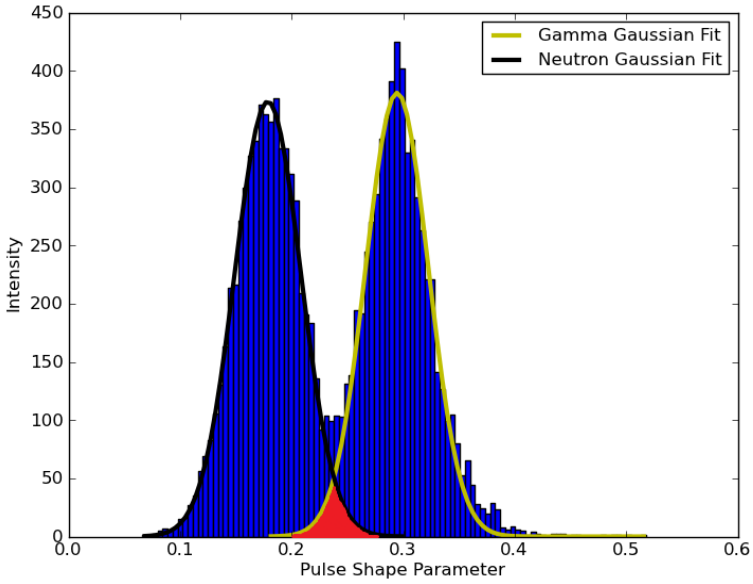

Figure 4-35: Curve Fitting Figure-of-Merit

The curve-fitting figure of merit shows that each Gaussian distribution fits well with the experimental data and the best-fit parameters and intersection point of the distributions are shown in Table 4-10.

Table 4-10: Curve Fitting Figure-of-Merit Parameters

Parameter	Gamma Gaussian	Neutron Gaussian
μ	0.2943	0.1784
σ	0.028	0.029
A	381.06	373.58
X_o	0.2378	

Using these parameters and evaluating equation (4.20) with the appropriate bounds, it was determined that the fraction of overlapping area under the Gaussian distributions, shaded in red in Figure 4-35, amounts to approximately 2.24% of the total area, thus the curve fitting PSD misclassified about 2.24% of the waveforms analyzed. The higher misclassification rate could be due to the fitting sensitivity to noise and better results have previously been obtained by using multiple decay constants; however, these fitting procedures are known to be much more computationally intensive [44].

The classifications made by the PSD and TOF measurement and the misclassification rate given by the figure-of-merit for each method are compared in Table 4-11.

Table 4-11: PSD Method Results Comparison

Classification	Charge Integration	Pattern Recognition	Curve Fitting
Gamma (%)	31.16	31.36	30.13
Neutron (%)	46.99	47.39	48.32
Delayed Gamma (%)	21.20	20.80	19.87
Noisy Pulses (%)	0.65	0.43	1.66
Particle Misclassification (%)	1.41	0.67	2.24

The table shows that each method shows agreement within 2% for each classification made. Based on these results and the figure-of-merit particle misclassification rate, the pattern recognition method was determined to show the best results; however, further investigation may show this conclusion to be misleading due the asymmetry of the neutron peak previously shown in Figure 4-34.

Chapter 5 -- Conclusions

The ability to quickly and accurately characterize special nuclear material is crucial in nuclear security applications. The shortage of ^{3}He has made it necessary to develop alternative neutron detectors. Liquid organic scintillators have the potential to replace ^{3}He detectors because of their sensitivity to fast neutrons, their pulse shape discrimination ability, and their fast time response. In this work the 500 MHz, 12-bit, Pixie-500 digitizer was coupled with EJ309 liquid scintillators to perform a bench-top ^{252}Cf time of flight experiment and analyze the waveforms with 3 separate PSD algorithms. The classifications given by the TOF experiment were compared to those made by the PSD methods. These methods included a digital charge integration technique, a pattern recognition method, and a curve fitting procedure. Each PSD method exploits pulse shape differences in a different manner but our results indicate good agreement among the different methods applied to the same data set; each method's classifications fell within 2% of the other two methods. The Gaussian fitting figure-of-merit analysis indicates that the pattern recognition method exhibits the lowest particle misclassification rate; however, this may be misleading due to the asymmetry of the neutron pulse shape parameter distribution exhibited by this method. The charge integration method exhibited a higher particle misclassification rate, but still under 1.5%, while the curve fitting method exhibited a misclassification rate just over 2%, probably due to the sensitivity of noise on the baseline of the pulse.

Future work could include an effort to resolve the shape of the neutron parameter peak from the pattern recognition method in order to obtain a better fit to experimental data than the Gaussian fit used in this work. A better fit would yield a more accurate misclassification rate for this method. Future effort could also be made to classify incoming radiation in real time. A study to determine if each PSD algorithm could be implemented in the Pixie-500's DSP or the FPGA would be beneficial.

References

1. "Treaty Between the United States of America and the Russian Federation On Strategic Offensive Reductions (The Moscow Treaty)." U.S. Department of State. U.S. Department of State, n.d. Web. 11 Feb. 2013.

2. "New START." U.S. Department of State. U.S. Department of State, n.d. Web. 11 Feb. 2013.

3. Orlov, Vladimir A. "Illicit Nuclear Trafficking & the New Agenda." IAEA.org. N.p., 2003. Web. 11 Feb. 2013.

4. "Nuclear Terrorism Fact Sheet," Harvard Kennedy School, http://www.nuclearsummit.org/files/FACT_SHEET_Final.pdf

5. "Special Nuclear Material." *NRC.gov*. N.p., n.d. Web. 28 Jan. 2013.

6. United States. Cong. Congressional Research Service. *The Helium-3 Shortage: Supply, Demand, and Options for Congress*. By Dana A. Shea and Daniel Morgan. Cong. Rept. N.p.: n.p., 2010. Web.

7. United States. U.S. Department of Energy. Alternative Neutron Detection Testing Summary. By R. T. Kouzes, J. H. Ely, and L. E. Erikson. N.p.: n.p., 2010. Print.

8. Tsoulfanidis, Nicholas, and Sheldon Landsberger. *Measurement and Detection of Radiation*. Boca Raton, FL: CRC, 2011. 178. Print.

9. Knoll, Glenn F. *Radiation Detection and Measurement*. New York: Wiley, 2000. 223. Print.

10. Knoll, Glenn F. *Radiation Detection and Measurement*. New York: Wiley, 2000. 224-25. Print.

11. Knoll, Glenn F. *Radiation Detection and Measurement*. New York: Wiley, 2000. 553. Print.

12. Knoll, Glenn F. *Radiation Detection and Measurement*. New York: Wiley, 2000. 561. Print.

13. Tsoulfanidis, Nicholas, and Sheldon Landsberger. *Measurement and Detection of Radiation*. Boca Raton, FL: CRC, 2011. 177. Print.

14. L.F. Miller, J. Preston, S. Pozzi, M. Flaska, J. Neal, "Digital Pulse Shape Discrimination," Radiation Protection Dosimetry, Volume 126, No. 1-4, pp 252- 255, (2007)

15. Knoll, Glenn F. *Radiation Detection and Measurement*. New York: Wiley, 2000. 226. Print.

16. "EJ-309." Eljentechnology.com. Eljen, n.d. Web. 1 Feb. 2013.

17. G. Ranucci, Nucl. Instr. Methods, Vol. A354, (1995) 389- 399.

18. M. Flaska, S.A. Pozzi, Nucl. Instr. and Meth. A (2008), doi: 10.1016/j.nima.2008.10.030

19. Knoll, Glenn F. Radiation Detection and Measurement. New York: Wiley, 2000. 680. Print.

20. Flaska, Marek, and Sara A. Pozzi. "Identification of Shielded Neutron Sources with the Liquid Scintillator BC-501A Using a Digital Pulse Shape Discrimination Method." Nuclear Instruments and Methods in Physics Research A (2008): 654-63. Print.

21. Bryan, William L., and Charles L. Britton. "Fast Neutron-Gamma Pulse Shape Discrimination of Liquid Scintillation Signals for Time Correlated Measurements." IEEE (n.d.): n. pag. Print.

22. Nakhostin, N., and P. M. Walker. "Application of Digital Zero-crossing Technique for Neutron-gamma Discrimination in Liquid Organic Scintillation Detectors." Nuclear Instruments and Methods in Physics Research A 621 (2010): 498-501. Print.

23. Takaku, D., T. Oishi, and M. Baba. "Development of Neutron-Gamma Discrimination Technique Using Pattern-Recognition Method with Digital Signal Processing." Progress in Nuclear Science and Technology 1 (2011): 210-13. Print.

24. M. Flaska, S.A. Pozzi, Optimization of an offline pulse-shape discrimination technique for the liquid scintillator BC-501A, Oak Ridge National Laboratory report, ORNL/TM-2006/120, 2006.

25. Lawrence, C. C., and M. M. Flaska. "21. Time-of-Flight Measurement for Energy Dependent Intrinsic Neutron Detection Efficiency." IEEE (n.d.): n. pag. Print.

26. Knoll, Glenn F. *Radiation Detection and Measurement*. New York: Wiley, 2000. 647. Print.

27. Knoll, Glenn F. *Radiation Detection and Measurement*. New York: Wiley, 2000. 648. Print.

28. Knoll, Glenn F. *Radiation Detection and Measurement*. New York: Wiley, 2000. 651. Print.

29. *User's Manual Digital Gamma Finder (DGF) Pixie-500*. Jan. 2011. CA, Hayward

30. "FPGA Fundamentals." *NI Developer Zone*. N.p., 03 May 2012. Web. 25 Jan. 2013. <http://www.ni.com/white-paper/6983/en>.

31. *User's Manual Digital Gamma Finder (DGF) Pixie-4*. Jan. 2011. CA, Hayward

32. Knoll, Glenn F. *Radiation Detection and Measurement*. New York: Wiley, 2000. 221. Print.

33. Chen, Hsin-Liang, Yi-Fang Huang, Chao-Ping Hsu, Tsong-Shin Lim, Li-Chung Kuo, Man-kit. Leung, Teng-Chih Chao, Ken-Tsung Wong, Show-An Chen, and Wunshain Fann. "Direct Measurements of Intersystem Crossing Rates and Triplet Decays of Luminescent Conjugated Oligomers in Solutions." *The Journal of Physical Chemistry A* 111.38 (2007): 9424-430. Print.

34. Knoll, Glenn F. *Radiation Detection and Measurement*. New York: Wiley, 2000. 230. Print.

35. Weisstein, Eric W. “Power Spectrum.” From *MathWorld*--A Wolfram Web Resource. http://mathworld.wolfram.com/PowerSpectrum.html

36. Knoll, Glenn F. *Radiation Detection and Measurement*. New York: Wiley, 2000. 49. Print.

37. Knoll, Glenn F. *Radiation Detection and Measurement*. New York: Wiley, 2000. 227. Print.

38. S. F. Naeem, S. D. Clarke, and S. A. Pozzi, "Validation of Geant4 and MCNPX-PoliMi Simulations of Fast Neutron Detection with the EJ-309 Liquid Scintillator," Nuclear Instruments and Methods, Section A, to be published 2013.

39. A. Enqvist, C. C. Lawrence, T. N. Massey, and S. A. Pozzi, "Neutron light output functions measured for EJ309 liquid scintillation detectors," Proceedings of the INMM 53rd Annual Meeting, 2012.

40. Knoll, Glenn F. *Radiation Detection and Measurement*. New York: Wiley, 2000. 660. Print.

41. Fallu-Labruyere, A., H. Tan, W. Hennig, and W. Warburton. "Time Resolution Studies Using Digital Constant Fraction Discrimination." *Nuclear Instruments and Methods in Physics Research Section A: Accelerators, Spectrometers, Detectors and Associated Equipment* 579.1 (2007): 247-51. Print.

42. Nuclear Instruments and Methods in Physics Research A 694 (2012) 119-125

43. International Journal of Applied Radiation and Isotopes, 1973, Vol.24, pp. 585-591. Pergamon Press. Printed in Northern Ireland. – cf neutron spectrum

44. S. Marrone, Nucl. Instrum. Methods, B213, 246 (2004)

45. Hamamatsu. *Photomultiplier Tubes: Basics and Applications*. 2006

Appendix

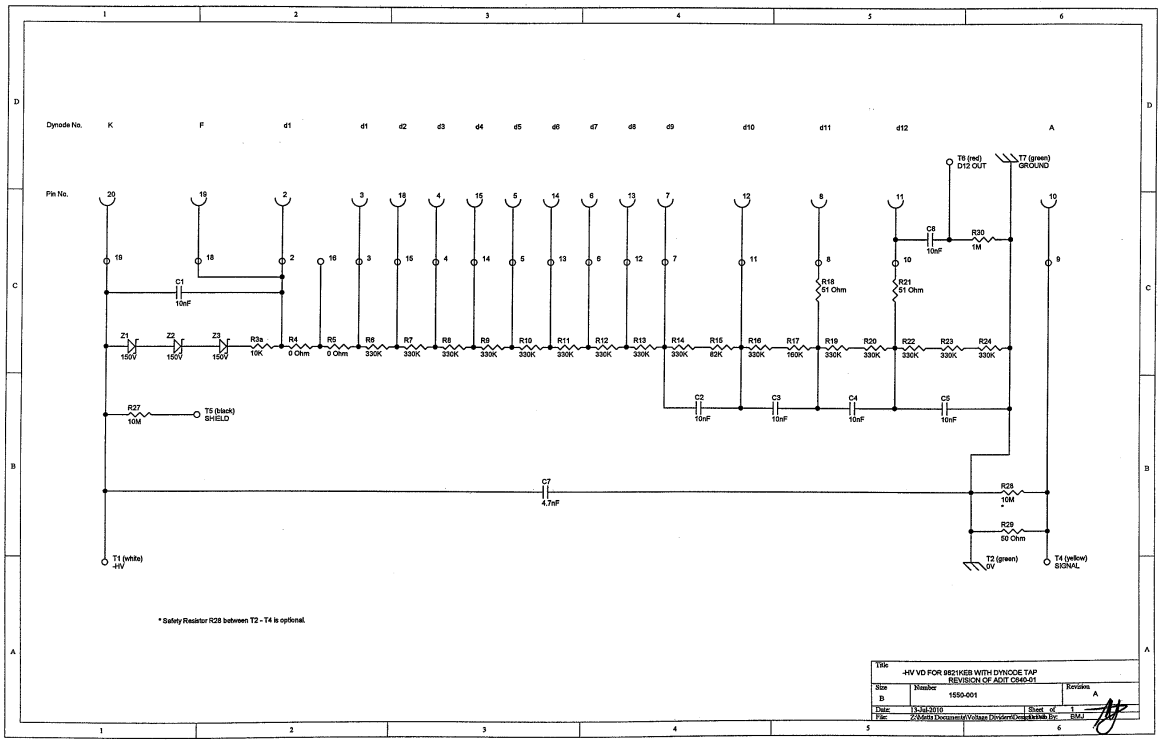

Figure A-1: 3x3 Etel Circuit Diagram

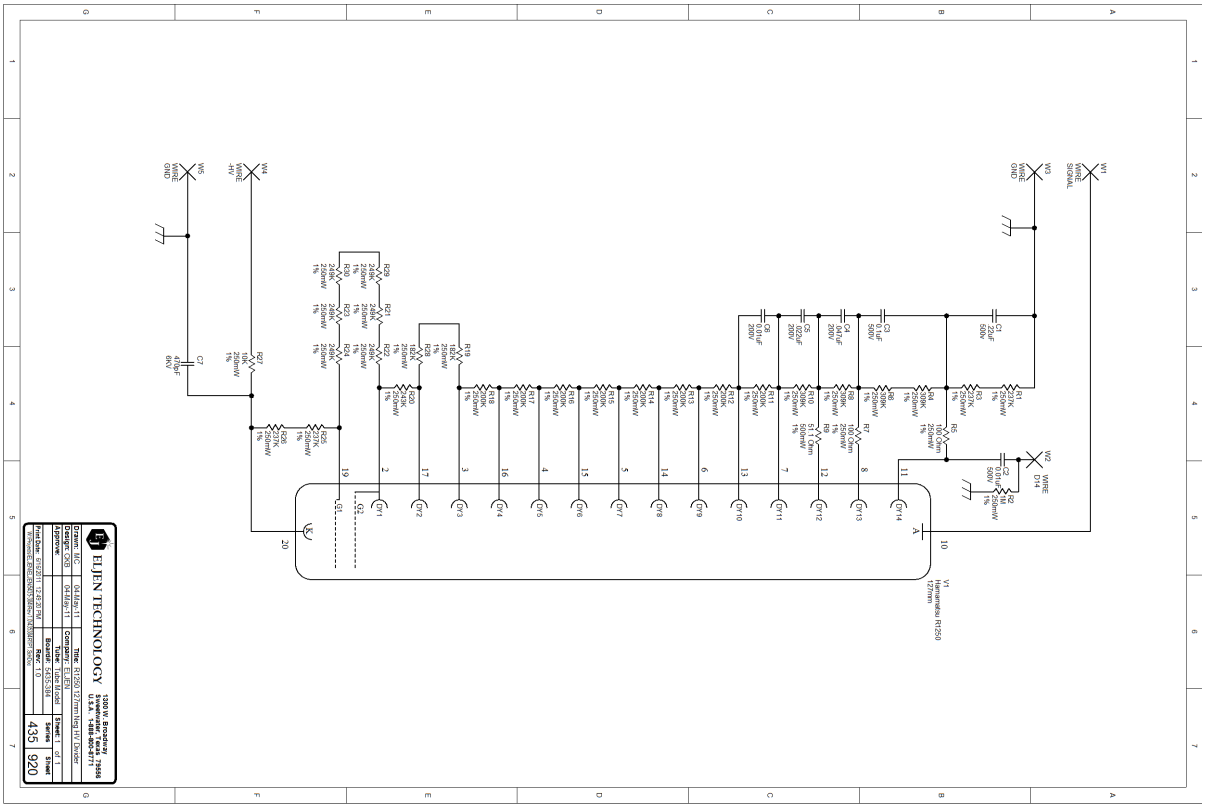

Figure A-2: 5x5 Hamamatsu Circuit Diagram

Figures A-1 and A-2 show the circuit diagram for the voltage dividers found in the 3x3 and 5x5 PMTs. These have been designed to reduce oscillations in the step response of the detector, i.e. ringing, through the use of several damping resistors. For waveforms that exhibit fast rise times (10 ns or less) inserting dampening resistors into the last several dynodes of the voltage divider has been shown to reduce ringing [45]. For the 3x3, resistors 18 and 21 are 51 ohms and serve as the damping components as shown in Figure A-1. For the 5x5, resistors 5, 7, and 9 serve as the damping resistors, which allow the signal the decay quickly without oscillation about the maximum.

EJ-309 LIQUID SCINTILLATOR
PULSE-SHAPE DISCRIMINATION PROPERTIES

This new liquid scintillator has been developed as an alternate to the more commonly used PSD liquid scintillators and is formerly known as EJ-399-06. The most well-known scintillator providing neutron-gamma discrimination is NE-213, and Eljen manufactures an identical equivalent, EJ-301. These are based on the solvent xylene which exhibits a high degree of solvent action and, with a flash point at 77°C, is rated as a flammable liquid. EJ-309 provides just slightly poorer PSD characteristics but does possess a number of chemical properties recommending it for use in environmentally difficult conditions.

- High flash point
- Low vapor pressure
- Low chemical toxicity
- Compatibility with cast acrylic plastics

PROPERTIES	
Light Output (% of Anthracene)	75%
Photons produced by a 1 MeV electron	11,500
Wavelength of Maximum Emission	424 nm
Decay Time, Short Component	approx. 3.5 ns
Bulk Light Attenuation Length	>1 meter
Specific Gravity (15°C)	0.959
Refractive Index n_D	1.57
Flash Point	144°C (291°F)
Boiling Range	(290-300°C)
Vapor Pressure (20°C)	0.002 mm Hg
ATOMIC COMPOSITION	
No. of H Atoms per cm^3	5.43×10^{22}
No. of C Atoms per cm^3	4.35×10^{22}
H:C. Ratio	1.25
No. of Electrons per cm^3	3.16×10^{23}

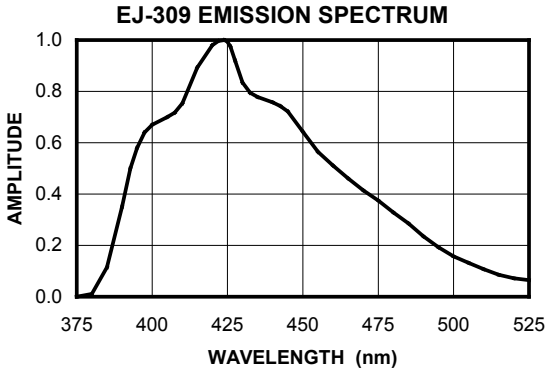

September, 2010

ELJEN TECHNOLOGY
1300 W Broadway
Sweetwater TX 79556 USA

Tel: (325) 235-4276 or (888) 800-8771
Fax: (325) 235-0701
Website: www.eljentechnology.com

Figure A-3: EJ309 Properties